Determination of Premixed Flame Characteristics by Tomographic PIV

ME55035 Msc Thesis

Jack Clarke

Technische Universiteit Delft

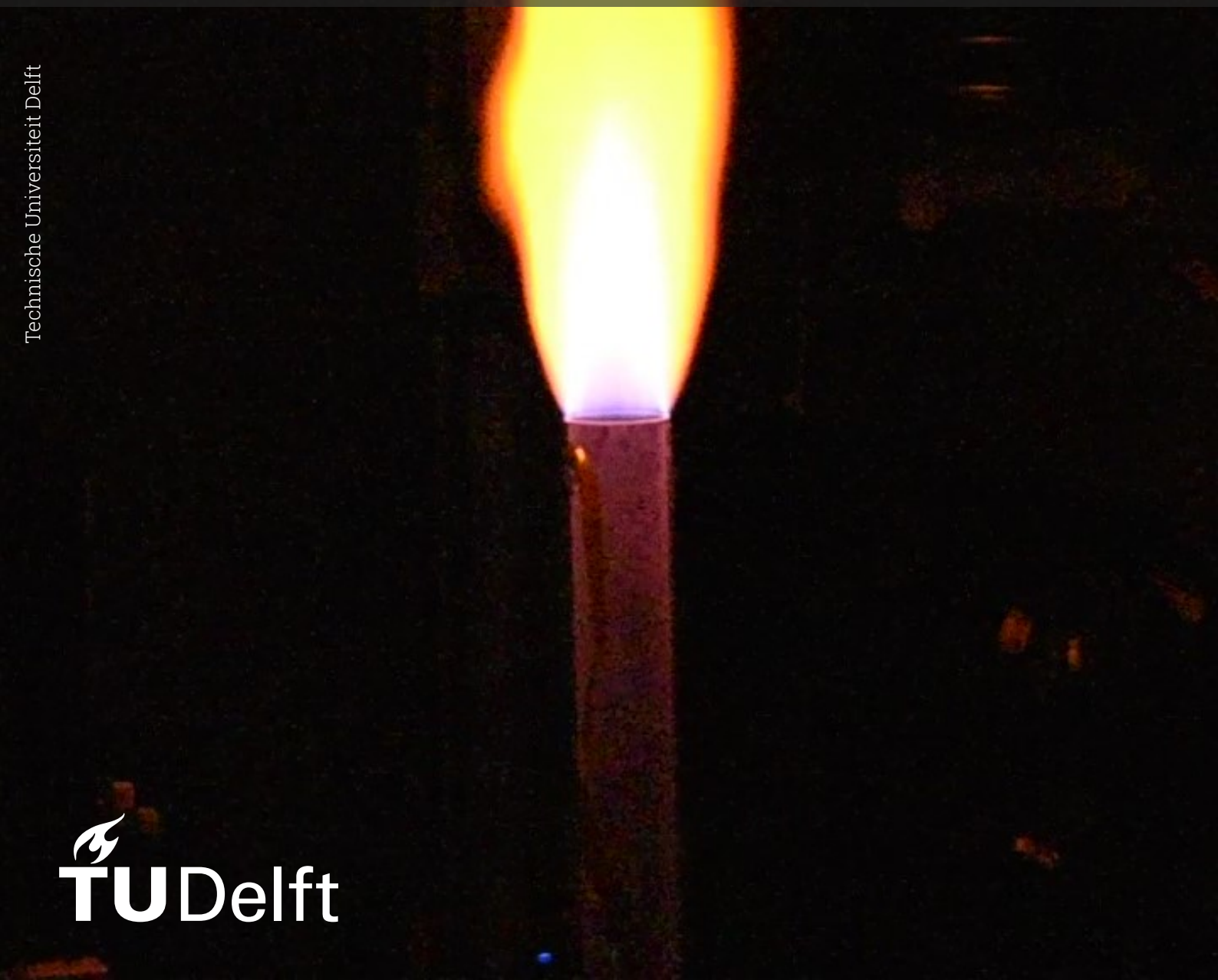

TU Delft

Determination of Premixed Flame Characteristics by Tomographic PIV

by

Jack Thomas Clarke

to obtain the degree of Master of Science

at the Technische Universiteit Delft,

to be defended publicly on Friday August 15, 2025 at 13:00.

Student number: 5861179

Project duration: April, 2024 – August, 2025

Thesis committee: Dr. Ir. G. E. Elsinga, TU Delft, Supervisor
Dr. Ir. M. J. Tummers, TU Delft, Supervisor
Prof. dr. F. Scarano, TU Delft, Examiner

Cover: Photo of a flame. Retrieved from https://stock.adobe.com/ under a free license.

Keywords: Turbulent burning velocity, Tomographic PIV, Tomo-PIV

An electronic version of this thesis is available at http://repository.tudelft.nl/.

TU Delft

Abstract

With global greenhouse gas emissions continuing to rise, there is a growing need to reduce the environmental impact of industrial processes. Much of these emissions are produced in the power and industrial processes industries. A common example of this is gas turbines where there is a focus on reducing the amount of pollutants emitted through regulation. With gas turbines operating on increasingly leaner mixtures of natural gas there is an interest in possible alternative fuel sources, such as hydrogen. However, the characteristics of hydrogen flame propagation are not well understood and therefore present an opportunity for research.

Modern combustion research relies heavily on CFD modelling, which depends on accurate physical parameters derived from experiments. One of the key quantities used in these models is the speed at which the flame propagates, the turbulent burning velocity. The turbulent burning velocity is difficult to measure due to its constant variability in both time and space. The goal of the work is to accurately and reliably locate the flame front and simultaneously measure the local flow instantaneous velocity.

As flames generally propagate in turbulent flows and turbulent flow is an inherently three dimensional phenomenon a three dimensional measurement technique was required. Tomographic particle image velocimetry (Elsinga et al., 2006) was chosen as the most effective way to simultaneously study the flame front location and the flow velocity field. A tomographic PIV setup was constructed using an expanded laser light sheet and several cameras, enabling the original 3D particle distribution to be reconstructed. Velocity fields were obtained by performing cross-correlation on sequential reconstructed volumes.

Premixed natural gas and air flames were predominately studied as they had a higher probability of success than hydrogen and air mixtures. Results found that both flame front detection and velocity field measurement could be conducted simultaneously on varying flame conditions. Flame front detection was found to be successful at high levels of seeding and could be validated by comparing to areas of high divergence in the flow field. Three dimensional velocity fields were verified using joint probability density functions of divergence and showed good results at all seeding levels. Data from experiments conducted on premixed hydrogen and air flames also yielded reliable flame front and velocity field data.

This study concludes that tomographic PIV is a viable method of studying flame front propagation and particularly the turbulent burning velocity in premixed combustion. Both natural gas and hydrogen fuelled flames produced accurate and validated results. Further work should include, the optimisation of experimental conditions for hydrogen flames and the improvement or more efficient deployment of lab resources. These efforts will support the development of more accurate combustion models and advance our understanding of hydrogen as a clean energy fuel.

Acknowledgements

With the conclusion of this thesis, I find myself at the end of my time at TU Delft. I am extremely grateful to have had the opportunity to study at such a prestigious university over the past few years. Before beginning my journey here, I was unsure if further studies were right for me. I am pleased to say that what I have learned has surpassed anything I could have ever imagined. I remain in awe of what engineering and science can do for this world, and I hope to continue contributing to the growth of a sustainable future.

Firstly, I would like to thank my supervision in this thesis Gerrit and Mark. Your enthusiasm and patience throughout this project allowed me to push the boundaries of what I thought was possible. Your introduction to Tomographic PIV made me ponder three-dimensional space and time in ways I never had before, and at times, my own place in it. I would also like to thank Rafael for your precise experimental work and insightful discussions throughout my thesis. Finally, I want to acknowledge the support staff at the P&E laboratory for their help in the construction of my experimental setup.

In addition, to my parents and siblings I am forever grateful for your never-ending support and reality checks. Thank you for listening to my never-ending stories and ramblings, regardless of how incoherent they were. This time spent pacing outside the library was more valuable to me and my belief in myself than I can put into words. To my girlfriend, thank you for your constant efforts to help me de-stress and for reminding me that life can also be enjoyed outside of work. And to the extended Gabriels family, for your warm hospitality - een hartelijke bedankt.

Finally, I would like to thank my friends and all the wonderful people I had the pleasure of meeting during my time in Delft. Particularly Ezra, Niko and Mo. Without your support I am certain that not only would I not have made it to this point but I would not have made it through half of the first year. Your countless hours of teaching, learning and credit-counting were instrumental to my success and I am forever in your debt.

There are many more I would like to thank personally, but I am rapidly running out of page. My time here at TU Delft has been truly fascinating, and I look forward to seeing where my newfound scientific curiosity will take me next.

Jack Clarke
Delft, August 2025

Table of Contents

List of Figures

List of Tables

Nomenclature

Abbreviations

Abbreviation	Definition
ART	Algebraic Reconstruction Technique
CCD	Charge-Coupled Device
CFD	Computational Fluid Dynamics
CMOS	Complementary Metal-Oxide Semiconductor
DOF	Depth of Field
DNG	Dutch Natural Gas
FOV	Field of View
GHG	Greenhouse Gases
IEA	International Energy Agency
IC	Internal Combustion
LOS	Line of Sight
MART	Multiplicative Algebraic Reconstruction Technique
MFG	Multiplicative First Guess
MLOS	Multiplicative Line of Sight
OH-PLIF	OH Planar Laser-Induced Fluorescence
PIV	Particle Image Velocimetry
PTE	Particle Tracking Enhancement
PTU	Programmable Timing Unit
PTV	Particle Tracking Velocimetry
RMS	Root Mean Square
SPIV	Stereoscopic Particle Image Velocimetry
UV	Ultraviolet

Symbols

Symbol	Definition	Unit
A	Area	m^2
c_p	Heat Capacity	$\mathrm{J\,kg^{-1}\,K^{-1}}$
C_{xx}	Normalized auto-correlation coefficient	[-]
d	Length Scale	m
D	Mass Diffusivity	$\mathrm{m^2\,s^{-1}}$
E	Measurement Light Intensity	[-]
f	Recording Frequency	kHz
$f_\#$	f-stop	[-]
I	Pixel Light intensity	[-]
k	Turbulent Kinetic Energy	$\mathrm{J\,kg^{-1}}$
l	Length Scale	m
l_k	Kolmogorov Length Scale	m
Le	Lewis Number	[-]
$\dot{m}$	Mass Flow Rate	$\mathrm{kg\,s^{-1}}$
M	Magnification	[-]
N_i	Number of Voxels	[-]
$\overrightarrow{n}$	Unit normal vector	[-]
P_k	Production of Turbulent Energy	$\mathrm{m^2\,s^{-3}}$
ppp	Particles per Pixel	[-]
Re	Reynolds Number	[-]
R_{xx}	Auto-covariance of velocity signal	$\mathrm{m^2\,s^{-2}}$
S_D	Flame Displacement Speed	$\mathrm{m\,s^{-1}}$
s_L	Laminar Burning Velocity	$\mathrm{m\,s^{-1}}$
s_T	Turbulent Burning Velocity	$\mathrm{m\,s^{-1}}$
t	Time	s
T	Temperature	$^\circ\mathrm{C}$
u	Velocity	$\mathrm{m\,s^{-1}}$
$u^{'}$	Velocity Fluctuations	$\mathrm{m\,s^{-1}}$
U	Velocity	$\mathrm{m\,s^{-1}}$
$\dot{V}$	Volumetric Flow Rate	$\mathrm{m^3\,s^{-1}}$
w_i	Weighting Coefficient	[-]
w	Velocity Component	$\mathrm{m\,s^{-1}}$
W	Laser Wavelength	nm
Y	Mass Fraction	$\%$
α	Heat Diffusivity	$\mathrm{m^2\,s^{-1}}$
ϵ	Viscous Dissipation	$\mathrm{m^2\,s^{-3}}$
τ_k	Kolmogorov Time Scale	s
θ	Cone Angle	$^\circ$
λ	Thermal Conductivity	$\mathrm{W\,m^{-1}\,K^{-1}}$
λ_T	Taylor Microscale	m
μ	Dynamic Viscosity	$\mathrm{kg\,m^{-1}\,s^{-1}}$
μ_s	Scalar Relaxation Parameter	[-]
ν	Kinematic Viscosity	$\mathrm{m^2\,s^{-1}}$
ϕ	Equivalence Ratio	[-]
ρ	Density	$\mathrm{kg\,m^{-3}}$

1

Introduction

1.1. Background

As is well publicised, global greenhouse gas emissions (primarily carbon dioxide, CO_2 and methane, CH_4) are still increasing worldwide. Despite this, there is some optimism that current trends are beginning to shift and that more renewable sources of energy are becoming increasingly viable (IEA, 2024). Recognising the problem, 196 countries and parties have signed up to the Paris Agreement in 2015, committing to do what was in their reasonable power to limit the average global temperature to a 1.5$°C$ increase from pre-industrialisation times (The United Nations, 2015). This mark is set as a level where the effects of climate change will be somewhat limited and not endanger a large proportion of the planet.

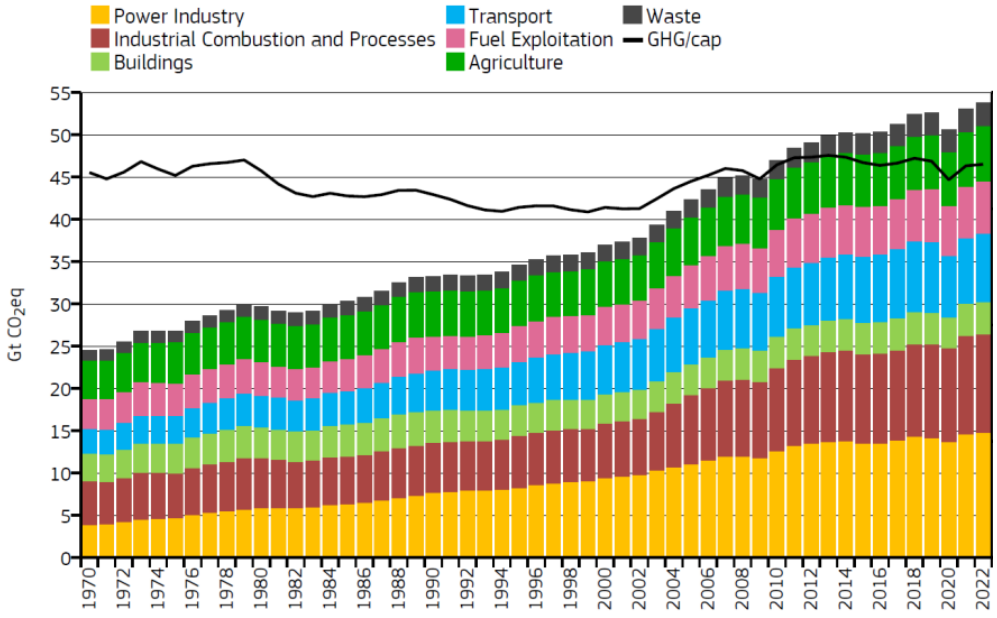

Figure 1.1: Global GHG emissions by sector over time. CO_2eq represents the global warming potential of all greenhouse gases in terms of CO_2 emissions. (European Commission, 2023)

As can be seen in figure 1.1, a large portion of these greenhouse gases (GHG) are produced in the power and industrial combustion and processes industries. These industries are often power intensive due to their need for heat. Heat generation itself comprises of more than half of the worlds energy consumption and cannot be easily replaced by renewable sources. Industrial processes like cement production or silicon wafer melting require combustion of a fuel source to achieve the necessary temperatures efficiently (IEA, 2024).

Combustion as a source of heat has been a part of humanity for hundreds of thousands of years. For its position as a fundamental part of everyday life we understand much less than might be expected of such a mature technology (Echekki and Mastorakos, 2011). In the past two centuries combustion engines have become a main source of energy for transportation, light and heat. Transportation is dominated by oil derived fuels which are combusted, accounting for 91% of consumption (Gragg, 2023). Furthermore, much of the supply of heat and power is generated by combustion in large gas turbines (IEA, 2024). These gas turbines produce large amounts of pollutants such as nitrogen oxides (NO_x) and carbon dioxide (CO_2) which are harmful to the climate and to humans. Therefore, governments are tightening regulations on these gas turbines in order to meet the climate goals previously discussed. Currently, gas turbines are operated with natural gas in a lean premixed mode to meet NO_x emission requirements, but relatively recent CO_2 emission requirements make hydrogen (H_2) an interesting fuel option. However, characteristics of flame propagation are not well understood in either natural gas & air mixtures or H_2 & air mixtures (Coriton and Frank, 2015). This presents a need to study flame propagation in more detail.

As flames generally occur in turbulent fuel-air mixtures there are some characteristics of the flow which cannot be studied with the standard 2D PIV methods. Turbulent flow is an inherently 3D phenomenon, it occurs at sufficiently high Reynolds numbers and has a wide range of time and length scales. Therefore, high-speed, 3D volumetric measurements are required to study flame propagation. Capturing the flame structure and its interactions with a turbulent flow, presents a measurement challenge (Coriton et al., 2014). Previous studies have investigated these quantities using multiple measurement techniques. Laser-Induced Fluorescence (LIF) is often employed to resolve the flame front, this technique works by imaging specific radicals produced around the flame front. The method is less reliable in practice as there is considerable smoothing required and LIF measurements are typically point measurements or planar measurements and inherently not three dimensional (Osborne et al., 2016). Additionally, the results of a successful PLIF measurement can then be matched to particle image velocimetry (PIV) data which measures the velocity field in a plane cross section of the flow. This in theory, allows for flame front behaviour to be fully studied (Trunk et al., 2013). This simultaneous use of two measurement techniques is complex without smoothing and the species being probed (often OH or CH radicals) do not indicate the exact flame front rather an adjacent plane (Osborne et al., 2016). With the proposition of Tomographic PIV (Elsinga et al., 2006), experiments have been conducted on flames where 3D velocity fields are recorded. Most experiments use PLIF measurements in combination with tomographic PIV to study flame propagation, which has previously discussed flaws and is limited to smaller depths of field (Coriton et al., 2014). Velocity measurements have been conducted to some success at larger depths of field (Tokarev et al., 2015) and separately, Mie scattering is proven as an equally viable technique for flame front imaging (Zheng et al., 2022). As previous studies have predominately focused on using Tomographic PIV as a qualitative addition to another experimental method, a quantitative measurement combining both velocity measurements and flame front imaging could represent a more reliable and straightforward method of studying flame propagation.

1.2. Research Objectives

As we move towards a carbon neutral world current combustion practices are being investigated for improvement opportunities. Burning hydrogen or the current natural gas based fuels in a more effective way could prove essential for reaching the previously stated climate targets. Currently, the main method of researching and modelling combustion is through large-scale CFD models. These models rely on certain physical parameters that can currently only be validated by experimentation (Mounaïm-Rousselle et al., 2013).

This thesis aims to add to this body of research by addressing two topics. To prove or discover the extent of the viability of tomographic PIV as a measurement technique on flames. And to measure one of the most important quantities in turbulent premixed combustion, i.e. the turbulent premixed burning velocity. With these topics, the research questions are formulated as;

- *How can Tomographic PIV be used to visualise and measure the flow velocity, while maintaining a highly accurate reconstruction?*

- *How can Tomographic PIV be used to detect the flame front of a flame?*
- *How can Tomographic PIV be used to measure the turbulent burning velocity of a flame?*

The simultaneous velocity and flame front measurement poses a challenge in that accurate tomographic velocimetry is typically associated with low to moderate concentrations of tracer particles (Elsinga et al., 2006, 2011) while flame front detection generally benefits from high concentrations (Altenburg et al., 2025).

1.3. Thesis Outline

The thesis will be presented in five chapters. Chapter 2 presents the theoretical background for the work, explaining the necessary theory of combustion as well as the measurement technique, tomographic PIV. In chapter 3 the experimental setup and methodology is discussed. Photos and descriptions demonstrate the equipment used and its functions and the experimental methodology is formed. In chapter 4 the results are presented and discussed. This chapter will examine what can be measured in combustion using tomographic PIV. Finally, in chapter 5 the initial research questions will be addressed again with the appropriate results.The discussion will work around the feasibility of the project and what research can follow on from it.

2

Theoretical Background

2.1. Combustion

2.1.1. Premixed Combustion

In premixed combustion the fuel and oxidiser are well mixed before combustion takes place. Once ignition is achieved, the resulting flame will continue to propagate into the mixture until nothing more can be burnt. A key quantity in premixed combustion is the equivalence ratio, ϕ. It is given by the actual ratio between the fuel and oxidiser and the stoichiometric ratio of the fuel and oxidiser

$$\phi = \frac{\dot{m}_{fuel}}{\dot{m}_{air}} \Bigg/ \left(\frac{\dot{m}_{fuel}}{\dot{m}_{air}}\right)_{ST}, \tag{2.1}$$

where $\dot{m}_{fuel}$ represent the mass flow rate of the fuel and $\dot{m}_{air}$ the mass flow rate of air. The subscript, ST represents stoichiometry. An equivalence ratio of 1, $\phi = 1$ represents stoichiometric combustion whereby there is exactly enough air to burn all fuel. An equivalence ratio of less than 1 is called lean or excess air combustion, whereby more air is present in the reaction than necessary to burn all the fuel. With more air present, the temperatures at which combustion occurs are lower than at stoichiometry and high thermal NO_x formation rates can be avoided. This is done to meet the NO_x emissions targets. Alternatively, an equivalence ratio of greater than 1 represents rich combustion where not enough air is present to burn all the fuel present.

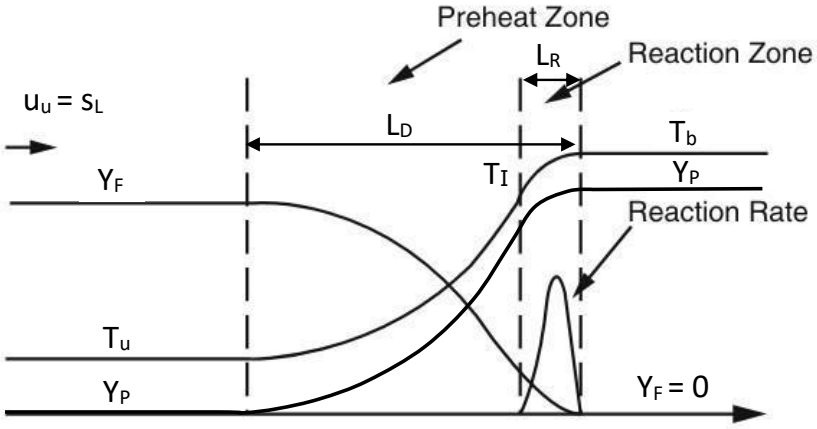

Figure 2.1: Temperature (T), Mass Fractions of fuel (Y_f) and reaction products (Y_p) of a stationary and one-dimensional premixed flat flame. The changes in the quantities over the x-axis represents the flow crossing the front (Hurley et al., 2016)

Figure 2.1 shows the profiles of the temperature (T), mass fractions of fuel (Y_f) and reaction products (Y_p) across a 1D premixed flat flame for lean combustion. The unburnt mixture at bulk velocity, u_u or the laminar burning velocity for a flat flame, s_L and the unburnt mixture temperature, T_u enter the preheat zone where it is heated but no combustion occurs. Once the mixture reaches ignition temperature, T_I the reaction occurs rapidly in the reaction zone. The mass fraction of the reactants, Y_F tend towards zero and the mass fraction of the products, Y_P increase. The burnt gas increases to its final temperature, T_b which is the adiabatic flame temperature assuming no heat loss (Law, 2006). The flame is described by two zones. In the preheat zone (L_D), the transport is governed by a balance of convection and diffusion. In the reaction zone it (L_R) is governed by chemical reactions and diffusion, as there is an abrupt change of properties in a short physical space. The relative magnitudes of the diffusion of heat and mass species is represented by the Lewis number

$$Le = \frac{\alpha}{D} = \frac{\lambda}{c_p \rho D}, \tag{2.2}$$

where α is the heat diffusivity, λ the thermal conductivity, c_p the specific heat capacity, ρ the density and D is the mass diffusivity of the mixture. A Lewis number of approximately unity is common for methane, but Le < 1 can be found for hydrogen and air mixtures (Peters, 2000).

Another quantity of interest is the flame thickness, which can be defined as the area over which the temperature and species change significantly and can be loosely approximated to the two zones previously discussed (Law, 2006). A simplification is often made as the reaction zone is generally much smaller than the preheat zone ($L_R << L_D$). Leading to the derivation of a simple model as convection and diffusion balance in the preheat zone

$$L_D = \frac{\lambda / c_p}{\rho_m s_L}, \tag{2.3}$$

where the thermal conductivity, λ and the heat capacity, c_p are taken in the fuel consumption layer where the fuel is consumed and the radicals are depleted. And density, ρ_m and the laminar burning velocity, s_L are taken in the unburnt mixture (Peters, 2000).

2.1.2. Laminar Premixed Combustion

In premixed combustion the burning velocity is a transport property that depends on the equivalence ratio, the temperature of the unburnt mixture, the pressure and the species in the mixture. It describes the intensity and ability for a flame to remain stable under varying flow conditions. It is commonly known as the velocity at which the flame front propagates relative to the unburnt gas mixture (Peters, 2000).

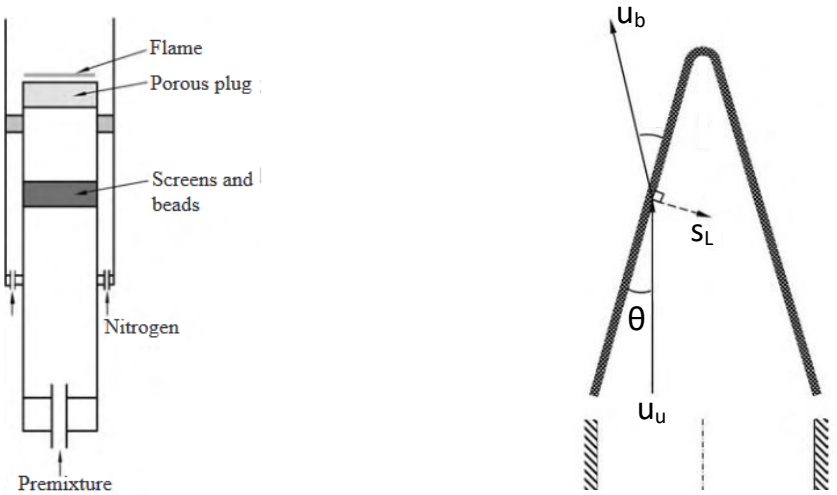

Figure 2.2: Flame fronts produced by different burners. On the left, the complete setup of a Flat-flame burner showing the flat flame front produced. On the right, the tip of a Bunsen burner and the oblique flame front produced by the burner. (Law, 2006)

Figure 2.2 shows the setup and flame front produced by a flat-flame burner (McKenna burner) and a laminar flame front produced by a Bunsen burner. A Bunsen burner works by inserting fuel into the base of the chamber, mixing it with air whose flow rate can be controlled by a varying inlet area and igniting. The unburnt gas mixture velocity is denoted by u_u, the angle any element of this flow makes with the flame front is given by θ and the burning velocity, the velocity of propagation normal to the flame front (on either side of the front) is given by s_L. The velocity of the burnt gases after they have crossed the flame front is u_b. The speed of flow can be controlled by constriction of the air inlet or gas flow. Once the flow from the Bunsen burner is higher than the rate at which the flow is burnt, a flame cone forms. The velocity of the flow increases across the flame front via the thermal expansion of the flame and the potential change in molecules from the reaction. The propagation of the flame was first measured by the "burner stabilised flame" method (Fine, 1957), where the flame speed s_L is related to the unburnt gas mixture velocity and the cone angle as in:

$$s_L = u_u \sin(\theta). \tag{2.4}$$

Under the assumption that the flame front is stationary in time, the angle formed by the bulk flow with the flame cone can be easily measured. The sin of this angle multiplied by the velocity of the bulk flow from the Bunsen burner is the laminar burning velocity, s_L.

A flat-flame burner has a premixed reactive mixture inserted to the flow chamber. A porous plug is used to achieve a uniform flow at the burner surface and produces a flat flame. Once ignition is achieved the flow rate can be adjusted to produce a steady, flat flame normal to the direction of flow. The burner is surrounded by a shroud of a relatively inert gas, such as nitrogen or argon. This shroud prevents perturbations in the flame surface and allows a good measurement of the flame surface area. The laminar burning velocity can be measured from this type of burner by

$$s_L = \frac{\dot{V}_m}{A_f} = \frac{\dot{m}_m}{\rho_m A_f}, \tag{2.5}$$

where $\dot{V}_m$ is the unburnt mixture volume flow rate, A_f is the surface area of the flame and the mass flow rate of the unburnt mixture is $\dot{m}_m$ (Law, 2006).

2.1.3. Turbulent Flow

Turbulent flows are ever present in the world and their study touches almost every topic. Most flows in combustion are turbulent due to the need for diffusion and higher burning rates. In order to understand the complex interactions of a flame and the flow we must look closer at turbulence. Turbulent flow is characterised by high Reynolds numbers. The Reynolds number represents the ratio of inertial and viscous forces in the flow.

$$Re = \frac{inertial}{viscous} = \frac{\rho \frac{U^2}{l}}{\mu \frac{U}{l^2}} = \frac{\rho U l}{\mu} \tag{2.6}$$

where U and l are macro scales for velocity and length, respectively and are determined by the geometry in which the flow occurs in. The inertial forces in a flow scale with $\rho u \frac{du}{dx}$ and the viscous forces scale with $\mu \frac{d^2 u}{dy^2}$. If the inertial forces become too strong or the viscous forces too weak then instability takes over and the flow becomes chaotic (Nieuwstadt et al., 2016).

Turbulent flow is also characterised by the presence of eddies, with the large scale turbulent eddies containing most of the turbulent kinetic energy. The turbulent kinetic energy is quantified as,

$$k = \frac{1}{2}\overline{u_i u_i} = \frac{1}{2}(\overline{u'^2} + \overline{v'^2} + \overline{w'^2}) \approx \frac{3\overline{u_o'^2}}{2}, \tag{2.7}$$

where $u_o^{'}$ represents the RMS of the fluctuations of a velocity component in the flow. Turbulent eddies break up into smaller eddies due to flow instability, smaller eddies also break up continuously

in what is called the cascade process. This process continues until velocity gradients are so large that viscosity starts to play a role, and the turbulent kinetic energy is dissipated into heat (Law, 2006). This occurs at the microscale which is the smallest scale in the flow and is characterised by the kinematic viscosity, $\nu = \frac{\mu}{\rho}$ and the viscous dissipation,

$$\epsilon \approx \nu \overline{\left(\frac{\partial u'}{\partial x}\right)^2} = \nu \left(\frac{U_{RMS}}{\lambda_T}\right)^2. \tag{2.8}$$

Where U_{RMS} is the RMS of the velocity fluctuations and λ_T is the Taylor microscale, an intermediate turbulence length scale. The production of turbulent kinetic energy is given by $P_k = -\overline{u_i' v_j' \frac{du_i}{dx_j}} \approx -\frac{u^3}{l}$. This energy production is equal to the energy going into the cascade effect. Therefore the turbulent kinetic energy production should balance the viscus dissipation and this gives another expression for the viscous dissipation rate,

$$\epsilon = P_k \approx \frac{u_o'^3}{l}, \tag{2.9}$$

where l is the integral length scale in the flow. At the end of the energy cascade process, viscosity begins to dominate the flow and turbulent eddies reach the smallest scale known as the Kolmogorov scale. The Kolmogorov length scale is the smallest length scale in the flow, l_k and the smallest time scale at play in the flow is the Kolmogorov time scale, τ_k defined as:

$$l_k = \left(\frac{\nu^3}{\epsilon}\right)^{1/4} \qquad \tau_k = \left(\frac{\nu}{\epsilon}\right)^{1/2}. \tag{2.10}$$

2.1.4. Turbulent Premixed Combustion

Turbulence enhances mixing during combustion. This leads to increased mass transport and fuel consumption, and therefore more heat being released by the reaction. The speed at which the flame propagates, the turbulent burning velocity is one of the most important quantities in modelling and predicting flame behaviour. The difficulty in determining the turbulent burning velocity lies in its instantaneous and local nature. At every point along the flame front the value of the burning velocity will be different due to the front's wrinkling and movements. Damköhler presented the first theoretical expressions for the turbulent burning velocity (Damköhler, 1940). His principle worked on the assumption of two turbulent regimes associated with the large scale and small scale respectively (Law, 2006).

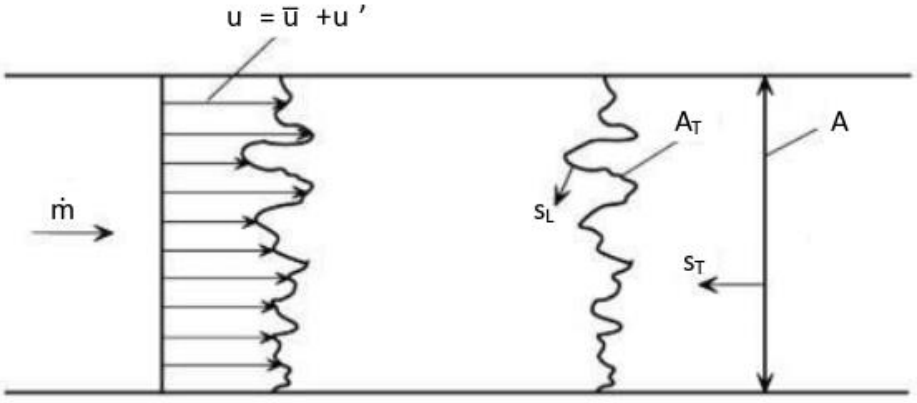

Figure 2.3: Schematic of a flame front in a constant area duct. The increased surface area caused by the wrinkling flamelets in the flame front illustrate Damköhler's theory for calculating the turbulent burning velocity, s_T. (Peters, 2000)

The theory of Damköhler is illustrated in Figure 2.3. In a theoretical constant cross section duct, the surface area, A of the laminar flame front would not change. In a turbulent flow where the turbulent eddies are larger than the flame thickness, there is substantial wrinkling of the flame front. This is

constituted by velocity fluctuations, u' over the mean velocity, $\overline{u}$. This increases the flame surface area to a new value, A_T. Mass conservation for a constant density flow through the increased flame front area gives

$$\dot{m} = \rho_u s_L A_T = \rho_u s_T A, \tag{2.11}$$

where ρ_u is the density of the unburnt mixture and s_L and s_T the laminar and turbulent burning velocities, respectively. Therefore, a relation between the turbulent and laminar burning velocity can be derived in terms of the increased area.

$$\frac{s_T}{s_L} = \frac{A_T}{A}, \tag{2.12}$$

where A_T/A will always be greater than 1, meaning that through turbulence induced flame wrinkling the turbulent burning velocity s_T is larger than the laminar burning velocity s_L. This relation allows us to understand the thin reaction zones better, as small scale turbulence transport is more complex.

2.1.5. Methods of Flame Front Displacement Measurement

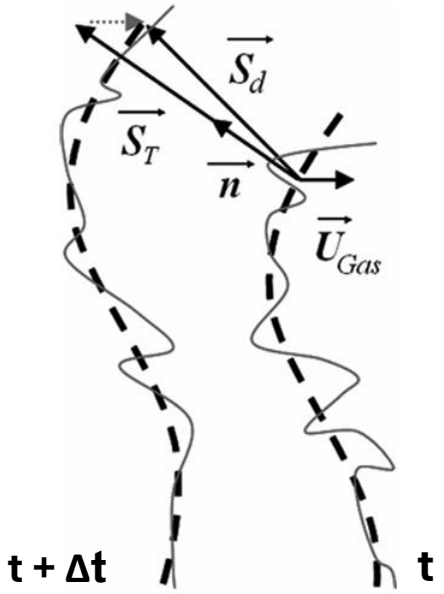

Figure 2.4: Visualisation of velocities that can be measured or calculated at a moving flame front. Solid weak grey lines indicate the wrinkled flame front and dashed heavy black lines show the average flame front position. Arrows indicate velocity vectors (Mounaïm-Rousselle et al., 2013)

Mounaïm-Rousselle et al. (2013) used the method depicted in figure 2.4 to determine flame propagation in an internal combustion (IC) engine cylinder. The experiment imaged flame propagation in a plane within the cylinder of an IC engine, using silicon oil seeding particles. In order to extract the turbulent burning velocity, $\overrightarrow{S}_T$ a high speed tomographic-PIV system was used. The fresh gas velocity, $\overrightarrow{U}_{gas}$ along the flame front contour is estimated by considering two tomographic images at different time instants with a small Δt set at 15µs. The instantaneous flame front propagation speed, $\overrightarrow{S}_d$ was measured in 2D, and as the flame fronts were not heavily wrinkled, the calculation hypothesis of the burning velocity was based on the small angle between velocity of the flame front and its normal direction. The threshold that minimises the weighted within-class variance was found and used to distinguish the unburnt and burnt zones by its particle density. The extracted flame contour was then filtered with a low pass filter to remove all structures smaller than the integral scale.

Equation 2.13 shows how the turbulent burning velocity was calculated. The velocity of the fresh gas was subtracted from the instantaneous velocity of the flame front. Both values are multiplied by the unit vector normal to the flame front, $\overrightarrow{n}$.

$$\overrightarrow{S}_T \cdot \overrightarrow{n} = (\overrightarrow{S}_d - \overrightarrow{U}_{gas}) \cdot \overrightarrow{n} \tag{2.13}$$

As the experiment was conducted on an engine cylinder there are extra complexities within the combustion chamber, mainly due the cyclic nature. To combat this, results were composed of time averaged velocities (Mounaïm-Rousselle et al., 2013).

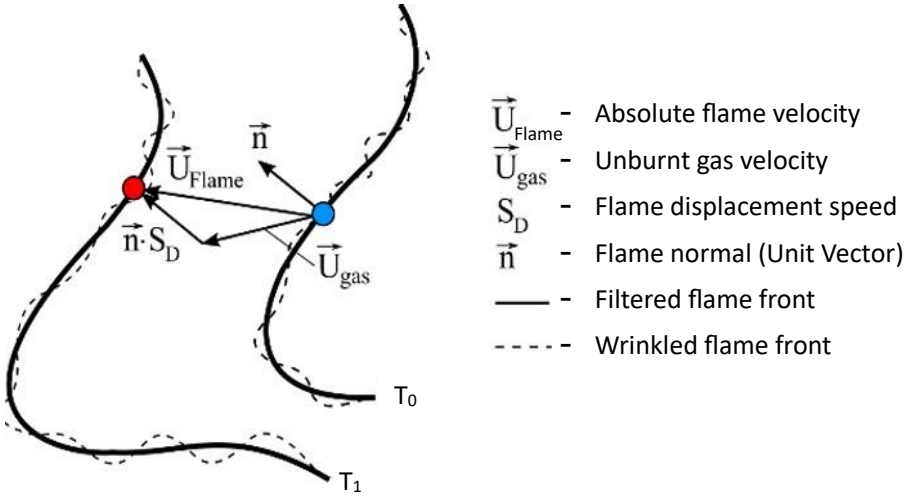

Figure 2.5: Visualisation of flame transport parameters around the flame front. Solid heavy black lines indicate the averaged flame front position and dashed weak grey lines show the exact flame front. (Peterson et al., 2019)

Peterson et al. (2019) also studied the turbulent burning velocity. Figure 2.5 displays the method used on an IC engine cylinder. The method used was first proposed using multi-plane OH planar laser-induced fluorescence (OH-PLIF) and stereoscopic particle image velocimetry (SPIV) to study 3D flame propagation (Trunk et al., 2013). It was then applied to an optical engine for a broad study of flame development (Peterson et al., 2015) and finally to study detailed flame transport and flame dynamics in an internal combustion engine (Peterson et al., 2019). The method works by imaging Hydroxyl (OH) radicals, which are produced after the flame has burnt an area. Thus, the maximum OH gradient is located on the burnt side of the flame front. Using a Canny edge detection algorithm the maximum OH gradient can be found and this becomes the identifier for the flame front.

The 3D flame surface between each OH plane is constructed using a spline interpolation and a patch diffusion algorithm removes noise from the reconstructed surface. To determine the displacement speed the flame front is moved in 3D space at t_0 by the local 3 component (3C) velocity. Then, the distance between the new front and the closest point on the reconstructed flame surface at $t_0 + \Delta t_{LIF}$ in the flame normal direction is measured. This distance divided by the time step (Δt_{LIF}) becomes the local displacement speed, S_D. The unburnt gas velocity, $\overrightarrow{U}_{gas}$ is extracted from the reconstructed images by tracking seeded particles.

$$\overrightarrow{U}_{flame} = \overrightarrow{U}_{gas} + S_D \overrightarrow{n} \tag{2.14}$$

Equation 2.14 shows the calculation of the absolute flame front velocity U_{flame}. It is defined as the sum of the local unburnt gas velocity, U_{gas} and the flame displacement speed relative, S_D to the flow in the flame-normal direction (Peterson et al., 2019).

A comprehensive review of turbulent premixed combustion found that turbulent burning velocities can be grouped into three distinct definitions (Driscoll, 2008). Global consumption speed is based on the theory presented section 2.1.2 for measuring laminar burning velocity. It is not suitable for measuring the quantities required here. Local consumption speed is generally used to identify the flame geometry, this approach is less favourable as it is more complex than necessary (Driscoll, 2008). Finally, the most common approach is the local displacement speed, equation 2.15. The local displacement speed is

a measure of the velocity of the flame fronts propagation and a version of it was used in (Mounaïm-Rousselle et al., 2013) and (Peterson et al., 2019).

$$S_{T,LD} = (U_{flame} - U_{gas})_{LE}\, n_{LE}. \tag{2.15}$$

where $_{LE}$ defines the leading edge of the flame front. The velocity of the gas into which the flame front is propagating, U_{gas} is subtracted from velocity of the flame in the laboratory reference, U_{flame} and the result is multiplied by the normal direction of the flame front.

In order to measure the turbulent burning velocity both U_{flame} and U_{gas} along with their angle to the normal direction must be measured. In the next sections we will discuss the best methods of measuring these parameters.

2.2. Visualisation (Particle Image Velocimetry)

Many early flow visualisation experiments were carried out before digital techniques were developed, notably by Prandtl (1936). Modern particle image velocimetry (PIV) was proven as a feasible method of visualisation in the 1980's by many, the work of Meynart (1983) was particularly important. Further improvements in the technology of lasers, sensors and computers over the years led to more advances. An excellent review of PIV is written by Adrian (1991) and a discussion of the principles and fundamentals is given by Westerweel (1993).

Recent developments in PIV have been driven by scientific research in the fluid- and aero-dynamic fields. Some modern books such as those written by Adrian and Westerweel (2011) and by Raffel et al. (2018) provide complete reviews of the majority of techniques and methods used in modern PIV, as well as many of the applications.

2.2.1. Working Principle

Figure 2.6 shows the working principle of PIV. Tracer particles are added to the flow in an area upstream of the interest area so the disturbance to the flow is minimised. The particles are illuminated in a defined area on the plane of interest by a pulsed laser. The light scattered by the tracer particles is recorded by a digital camera and stored on a computer. Two images recorded at two distinct times are cross-correlated to determine particle displacement between the recordings which is a measure for local flow velocity.

In a PIV experiment, some practical considerations have to be made. The recording systems must be calibrated. Seeding density must be large enough to allow resolving of the flow structures as well as operation of the algorithm. The particle size should be large enough to scatter light for an accurate recording of that image but also sized suitably to follow the flow exactly. The light source should illuminate the flow regions of interest. Finally, a consideration should be made as recording at high digital resolution often results in low temporal resolution and vice versa due to hardware limitations.

As a turbulent flame is an inherently three dimensional phenomenon we will investigate one with a 3D method of PIV. Due to advances in technology more advanced algorithms have been developed which can decipher three dimensional flow velocity. Over the years, many methods have been developed in order to track the motion of particles in three dimensions.

Holographic PIV uses an interference pattern from a second wave (the reference wave) and scattered light from particles which is recorded onto a photographic plate (hologram). The hologram is illuminated to reproduce the original light intensity field (Hinsch, 2002). The reconstructed particle distribution is scanned for a digital version of the intensity map. The main drawback here being that the images must be developed on photographic plates. This process is expensive and time consuming as plates must be managed by hand (Scarano, 2012). Digital holographic PIV has been proposed where the light pattern is now recorded directly onto the CCD camera sensor (Pan and Meng, 2002). As the interference light is being imaged directly onto the sensor the spatial resolution is limited by the physical size of the sensor. This makes it very difficult to image any large flow structures. Furthermore, in order to achieve acceptable resolution of the image a small viewing angle is needed due to the large distance between pixels (pixel pitch) (Hinsch, 2002).

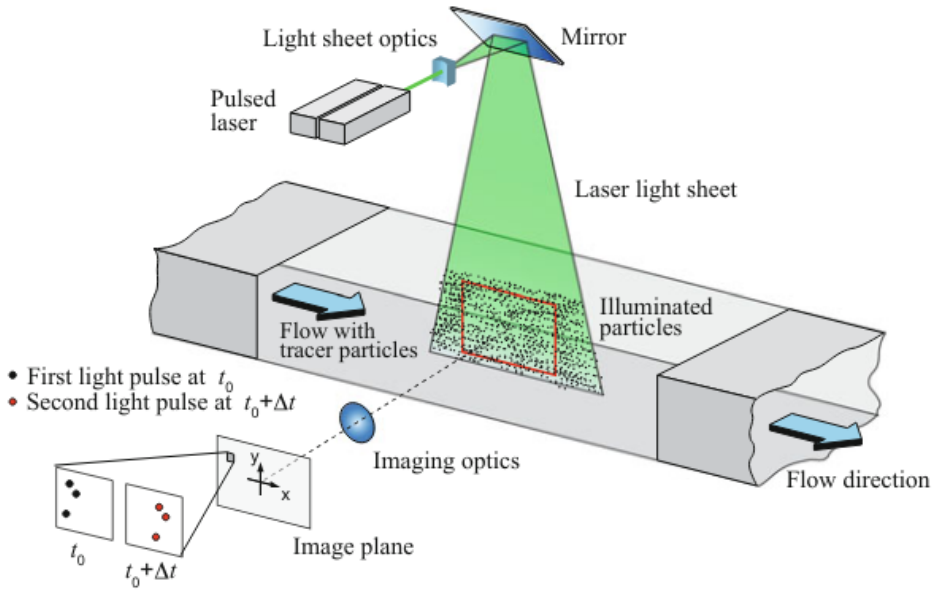

Figure 2.6: Schematic of a 2D-2C PIV Experiment. The top of the figure shows a PIV experiment conducted on flow in a channel and the bottom of the figure illustrates the process of image cross-correlation. (Raffel et al., 2018)

Stereo-PIV combines standard 2-component (2C) PIV with the principle of stereoscopy in order to add depth to a two dimensional image (Raffel et al., 2018). The displacement of the seeding particles is measured from two different viewing angles along the same plane of view. This allows all three velocity components to be captured simultaneously (Arroyo and Greated, 1991). In dual plane stereo-PIV (DSPIV) the setup is similar but now two separate, parallel light sheets using two separate stereo-PIV systems to image the same flow are used. Each set of cameras is setup to image differently polarised light, allowing the two systems to separate the images from the two planes. This allows all three velocity components to be measured (Wernet et al., 2016). The method is again limited as to add more planes would require adding more light colours and complicate the setup further (Elsinga et al., 2006).

The Scanning Light Sheet (SLS) method works by recording many separate 2D slices of a volume. This is often done using a mechanical device to slightly alter the position of the light sheet with the speed of the recording system. The images are combined into a 3D reconstruction of the original object. As each sheet is recorded as a separate image, the seeding density (and therefore spatial resolution) of the flow can be higher than other 3D techniques (Brücker, 1995). For displacement calculations the second image can be recorded directly after the first or after the whole volume has been recorded. Either method requires a high frequency laser which decreases the power of illumination and high frequency cameras. This limits the technique to flows with lower velocity to satisfy the 'frozen flow' condition (Lawson and Dawson, 2014).

Plenoptic PIV extends from the idea that plenoptic imaging is able to study the space from image to lens and reconstruct the path of the enclosed light rays. It works by placing a micro-lens array between the object and the sensor in order to collect spatial and angular information. Due to the smaller size of lens and sensors it is generally used to image larger depths (Rice et al., 2018).

Finally, 3D Particle Tracking Velocimetry (PTV) is based on identifying individual tracer particles within a flow and their coordinates. A Lagrangian algorithm then tracks the particles. The particle identification, coordinate determination and matching is a difficult and sensitive process which limits the number of particles that can be seeded as to avoid ambiguities (Maas et al., 1993). Multiple cameras are used (3-4) to find the coordinates of seeded particles. Particles are identified by triangulation. Exact triangulation is difficult to achieve in reality and a tolerance criterion is often employed. Furthermore, as each particle is tracked individually in the 3D PTV algorithm the seeding density generally is lower than in 3D PIV (Fu et al., 2016). Novel methods of particle tracking such as 'Shake-The-Box' offer

improvements in particle image density. The method makes use of a novel 'shaking' algorithm to create a more efficient reconstruction method. The algorithm produces an accurate guess of the particle distribution in a domain and 'shaking' the particles until an optimal distribution is achieved (Schanz et al., 2013).

2.2.2. Tomographic PIV

Figure 2.7 illustrates the equipment and reconstruction process of a Tomographic PIV (Tomo-PIV) experiment. Tomo-PIV has been proven effective for many non-intrusive types of measurement. Tt has been used to record flame propagation by studying flame structures (Osborne et al., 2016). It has been demonstrated that the flame front can be imaged by evaporation of particles (Ebi and Clemens, 2016) and in limited areas using the difference in density of solid particles (Osborne et al., 2016).

Working Principle

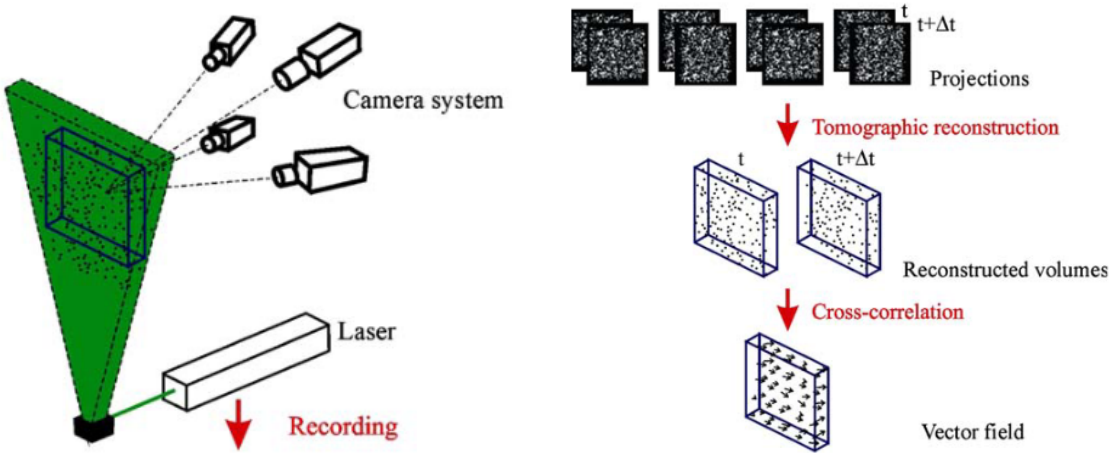

Figure 2.7: Schematic of the Tomographic PIV working principle. On the left a flow illustrated by a laser light source with 4 cameras used to capture images. On the right the process of image cross-correlation and tomographic reconstruction is illustrated. Resulting in a three dimensional velocity field (Elsinga et al., 2006)

Tracer particles are added to the flow upstream of the volume of interest to minimise their disturbance on the flow. The laser light sheet is expanded to provide volume illumination. The f-stop of the lenses is optimised to image the whole depth of the volume of interest and adaptors are used to meet the Scheimpflug condition. The scattered light is recorded by several cameras which view the same volume from different directions. The camera sensors feed the tomographic reconstruction which recreates the particle distribution within the measurement volume (the object) as a light intensity distribution. The reconstruction is done by a tomographic algorithm which uses the simultaneously recorded images from each camera and the calibration which provides the relation between the image space and the physical space in the measurement volume. Particle displacement (hence velocity) can be determined by 3D cross-correlation of two reconstructed volumes.

Reconstruction Algorithm

The novel aspect of Tomo-PIV is the 3D particle reconstruction algorithm using tomography. The algorithm uses a-priori knowledge about the imaging system and its relation to the object (i.e. the measurement volume). This information is obtained by a calibration done prior to the experiments and a volume self-calibration using the recorded data (Wieneke, 2008). Algebraic methods are preferred to analytical methods due to the discrete sampling of particles and the limited number of views (cameras). The iterative nature of algebraic methods handles this better (Elsinga et al., 2006).

The measurement volume containing the particle distribution (the object) is divided into a 3D array of cubic voxel elements in (X, Y, Z) with intensity (E). The light volume intensity from the measurement (E) is projected onto an image pixel (x_i, y_i) and returns the pixel intensity (I), written in equation 2.16.

$$\sum_{j \in N_i} w_{i,j} E(X_j, Y_j, Z_j) = I(x_i, y_i) \tag{2.16}$$

Where N_i represents the voxels that contribute to the image intensity of the i^{th} pixel. The weighting coefficient, $w_{i,j}$ expresses the contribution of the j^{th} voxel to the i^{th} pixel resulting in pixel intensity (I). The calculation is made with the line of sight evaluated as a cylinder and the voxels as spheres (Elsinga et al., 2006).

The multiplicative (multiplicative algebraic reconstruction technique) MART (equation 2.17), is the most commonly used base algorithm, which updates E accuracy to;

$$\begin{aligned} \textbf{MART} : & E(X_j, Y_j, Z_j)^{k+1} \\ & = E(X_j, Y_j, Z_j)^k \left(\frac{I(x_i, y_i)}{\sum\limits_{j \in N_i} w_{i,j} E(X_j, Y_j, Z_j)^k} \right)^{\mu_s w_{i,j}} . \end{aligned} \tag{2.17}$$

Where μ_s represents the scalar relaxation parameter (Scarano, 2012). Beginning with an initial guess E$(X_j, Y_j, Z_j)^0$ the object intensity value is updated iteratively. The MART method is updated by the ratio of the measured pixel intensity and the projection of current object. MART is dependent on the weighting coefficient as it is set to the exponent of the ratio. Therefore, only elements that have a nonzero coefficient will be updated. The MART methods acts as an AND operator, an individual voxel will only have a nonzero intensity if a particle is detected along all lines of sight (LOS) that intersect that voxel (Elsinga et al., 2006). The tomographic reconstruction is a naturally underdetermined problem as a single set of 2D projections can give multiple different 3D objects. A drawback of the MART reconstruction technique is the number of voxels which require computation, decreasing this computational load is achieved by using other reconstruction methods concurrently.

The additive (algebraic reconstruction technique) ART method is similar to MART but is updated with the residual of the measured pixel intensity and the projection of the current object. It acts as an OR operator: if a particle is detected within a voxel then all voxels along that LOS will become nonzero (Elsinga et al., 2006). The multiplicative first guess (MFG) method is based on the theory that much of the recorded area will not have any particles to be examined. The algorithm identifies large areas in the reconstruction volume which have zero or negligible intensity and discounts them (Worth and Nickels, 2008). The multiplicative line of sight (MLOS) method was developed by expanding on the original work of MFG (Atkinson and Soria, 2009). The particle tracking enhancement (PTE) method augments the initial guess used in a MART algorithm reconstruction. Using a cross-correlation from already reconstructed recordings and the object deformation technique, a more accurate initial guess is developed (Novara et al., 2010).

Finally, more modern development of flow field reconstruction combines the instantaneous flow field with the governing equations of fluid mechanics by data assimilation. 'Vorticity-in-cell plus' (VIC+) uses a form of Navier-Stokes equations to resolve flows at smaller scales than previously possible (Schneiders and Scarano, 2016).

2.3. Flame Front Detection

The flame front detection method will be illustrated using an example of a successful dataset from the experiments. The experiments and their results will be discussed thoroughly in the following chapters. Once images have been recorded and pre-processed, tomographic reconstruction is carried out in the Davis platform. The reconstruction volume is stored by Davis as a sequence of two dimensional planes. These planes are read into Matlab using a conversion function supplied by LaVision and then arranged such as to recover the reconstructed volume. The volume is then processed in Matlab.

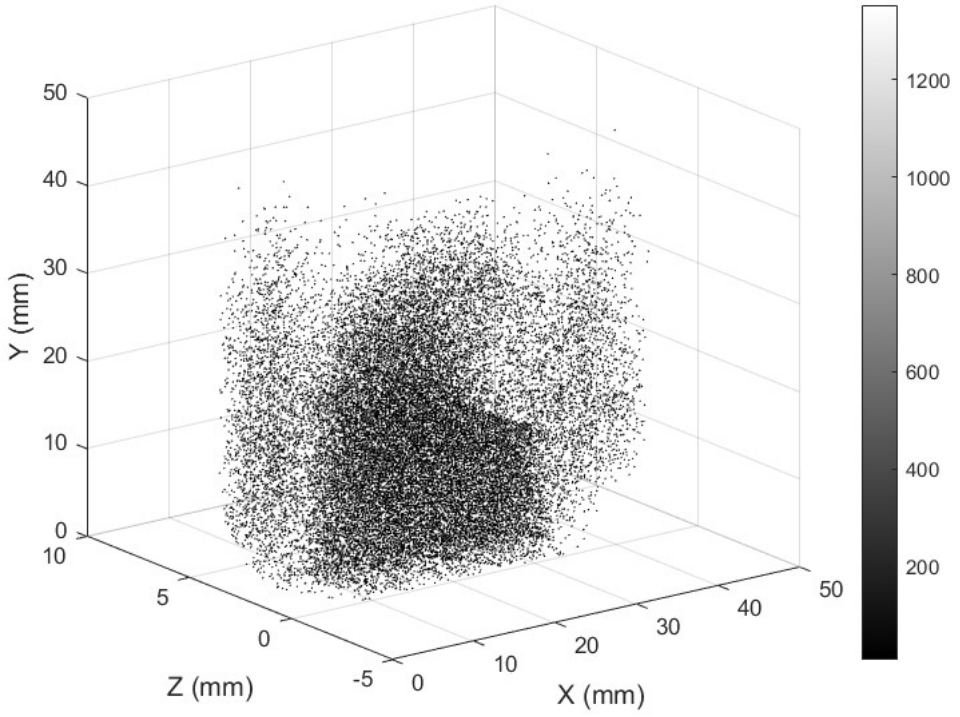

Figure 2.8: A full three dimensional flame image particle reconstruction. The grey scale bar represents the intensity of the reconstructed particles. The unburnt region region can be identified as the central heavily seeded area and the edges with less seeding are identified as the burnt regions. The image is taken from a run with medium seeding ($0.028ppp$) and time separation (Δt= 180 µs).

First a function identifies local maxima via Matlab's built in local maxima function. The maxima are verified for a 3x3x3 windows and then declared a particle. The declared particles and surrounding pixels are then fit to a gaussian function to create smooth, identifiable particles. The three dimensional coordinates of these particles and the intensity of each pixel in the particle are then stored. These coordinates can then be used to reconstruct a volume field in Matlab as seen in figure 2.8. The process is then repeated for the second frame giving two volume reconstructions for two correlated images.

Once a complete three dimensional object is reconstructed, the particle number density method is applied to find the flame front (Ebi and Clemens, 2016). This method works by discretising the volume into windows, and counting the number of particles in each windows. If the number of particles counted in a certain window are above the threshold then the window is still within the unburnt region of the flame. The window size that was used for this is 20x20x20 voxels (0.745mm^3) and there is a 50% overlap applied to the windows. This process results in a data set containing the number of particles in each window, and a binarised set containing which windows are over the set threshold. This is displayed in figure 2.9 in two dimensional cross-section, later many two dimensional planes are combined to form a three dimensional surface.

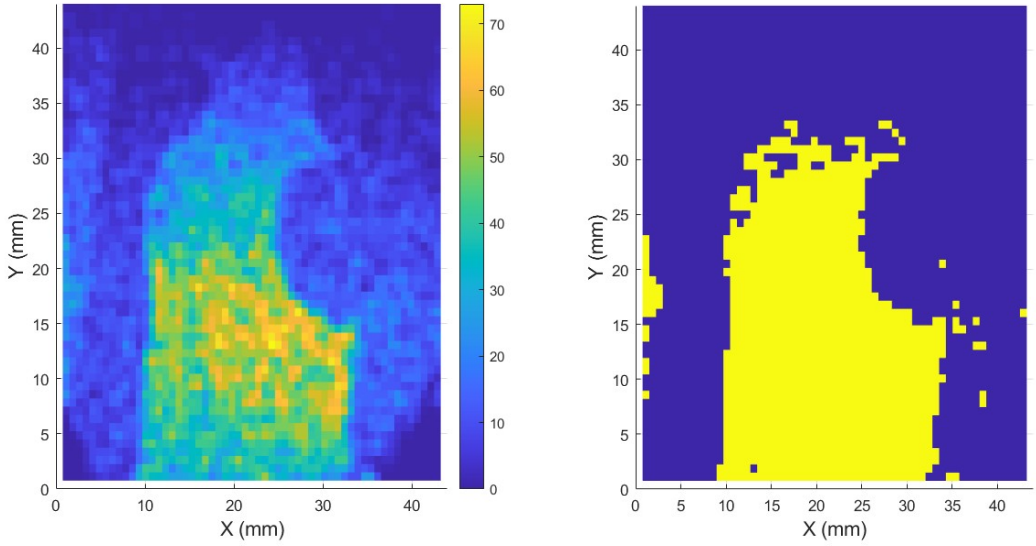

Figure 2.9: The flame front identification method. On the left, a two dimensional slice of the flame showing the number of particles contained within each window, the colour bar indicates the number of particles within a window. Windows are 0.745mm cubes with 50 $\%$ overlap applied. On the right, the same two dimensional slice binarised by a threshold of 20 particles (medium seeding - $0.028ppp$) . This represents the initial flame front identification before processing.

The binarised two dimensional slices are then processed to extract the flame front. Initially, a dilation filter is applied over a small window to fill any gaps in the image and connect some areas around the flame front. Then the largest continuous area is chosen to prevent large areas of reconstruction noise away from the front affecting the result. In the original images the base of the flame is located at the tube nozzle. This results in noise at the base of some images and the particle counting is not as reliable. To combat this the bottom row of particles in the image are padded and the flame shape is closed. Finally, an erosion filter is applied to the front, this is done to reduce the extra area that had been added at the edges by the dilation filter. The final result of this process can be seen as a binary image in figure 2.10.

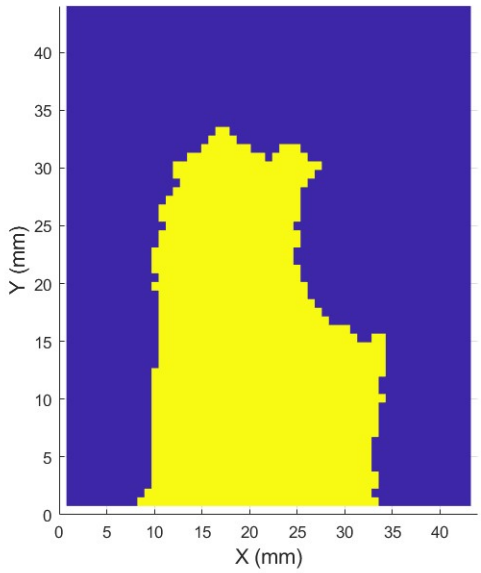

Figure 2.10: A two dimensional slice of the final flame front. The image is dilated, padded, the largest single shape is identified and finally eroded to restore the front to its original size. The image is taken from a run with medium seeding ($0.028ppp$).

Once all two dimensional slices from the volume have passed through this process, they can be combined to plot a flame surface. Figure 2.11 shows a three dimensional surface plotted over a three dimensional particle reconstruction. The surface is plotted from the edges of the binarised voxels. For the current window size the particle threshold used varies for the level of seeding. At the medium level the threshold is 20 particles but at the high level a threshold of 40 is used for effective reconstruction of the flame fronts.

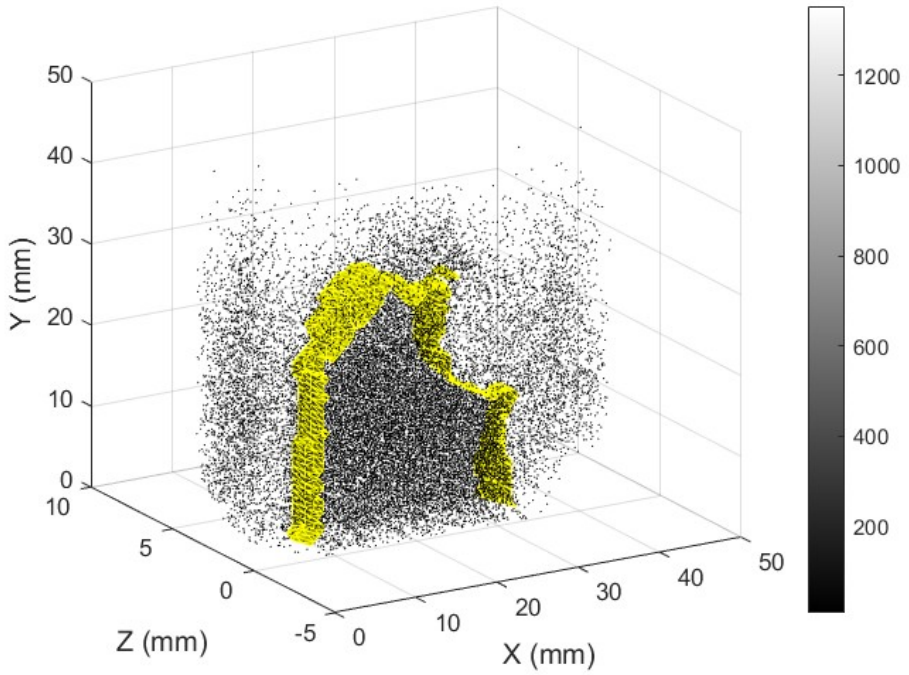

Figure 2.11: Combination of multiple two dimensional slice of front into a three dimensional front. The particles taken are shown as black dots with the grey scale bar representing intensity and the yellow surface represents the flame front.

3

Experimental Setup

This chapter discusses how the experiment was set up from the combustion side (section 3.1) and the tomographic PIV side (section 3.2). The former introduces the combustion facility and presents the burner configuration. The tomographic PIV discussion pertains to the setup of the cameras and the systems used to process the data. This explanation of the setup is provided so the reader can interpret the results of the experiment. This discussion is followed by the experiment methodology and the different cases that were studied.

3.1. Bunsen Burner Setup

The flame is generated by a classic Bunsen burner, as can be seen in figure 3.1. The fuels and air levels are controlled by mass flow controllers (1) and mixed in the pipe (3). They are then ignited as the mixture reaches the top of the quartz tube (6), which has an inner diameter of 26mm. The flow at

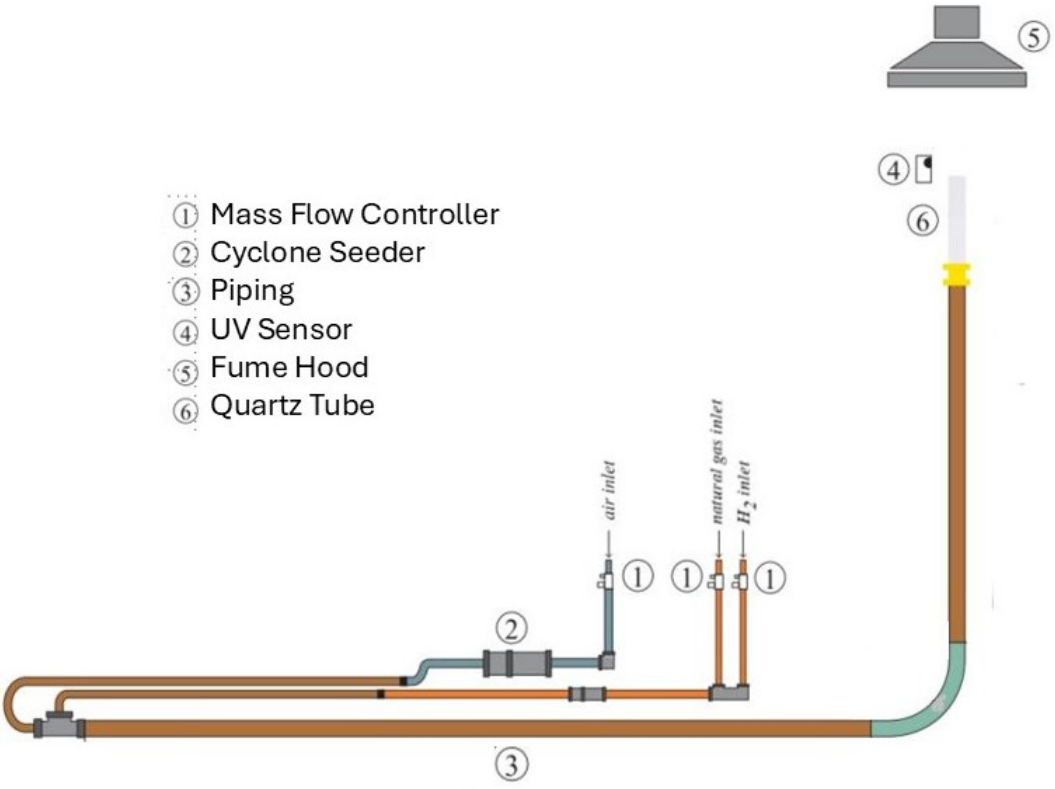

Figure 3.1: Bunsen burner setup schematic. Number scheme indicates use of items in setup. (Faldella, 2020)

the exit of this tube is a fully developed turbulent pipe flow for all the experiments. The seeding is provided through the cyclone seeder (2). The fumes generated by the burner are exhausted by the hood (5) and the lab safety network uses a UV sensor (4) to keep fuel flowing while the flame is lit. The mixture was ignited with a safety lighter.

The flow is seeded by a cyclone seeder, which is shown in figure 3.2. Air is forced directly into the seeder which causes the particles to be distributed throughout the seeder chamber. Seeding flows through a hole in the top of the seeder chamber and into the main pipe network where it is mixed with the fuels. In order to control the levels of seeding, valves are used to bypass the seeder chamber. Via careful control of these valves, the amount of seeding could be controlled and a safe pressure maintained in the chamber. This is not an entirely precise method and is noted as a source of seeding density fluctuations. The flow was seeded by 1-micron polishing alumina particles and Aerosil R972 was used as an anti-clogging agent to achieve an equal distribution of the particles in the flow.

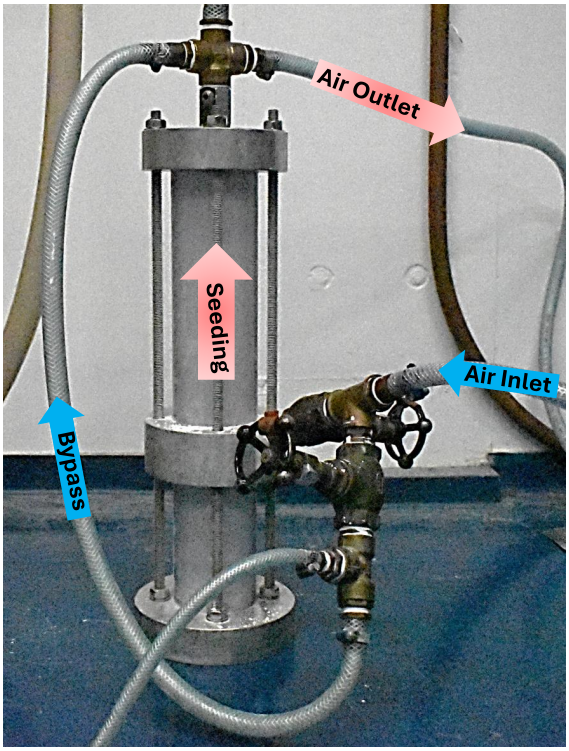

Figure 3.2: Picture from laboratory of the cyclone seeder used in experiments to seed airflow. The valves used to control the airflow can be seen at the bottom of the image. Arrows indicate airflow in the system, blue indicates unseeded air and red indicates air mixed with seeding.

The air and fuel flow was managed by Bronkhorst® mass flow controllers. These controllers allowed the flame conditions to be controlled to prevent a blow-off or flashback. They also allow for smooth transition from one experimental condition to the next. The controllers were controlled via a LabView panel. A panel is built with a graphical interface and this allows safe control of flame generation, while collecting relevant experimental data.

3.2. Optical Arrangement

The experiment was conducted with four high speed CMOS cameras placed in a rectangular configuration, as displayed in figure 3.3. The cameras are LaVision Imager Pro HS 4M's which have a pixel pitch of 11µm, a chip of 2016x2016 pixels and a corresponding image acquisition rate at full frame of 0.64 kHz in dual frame mode. The camera viewing directions are all approximately 30° normal from the light sheet in the horizontal off-axis angles. The stand off distance (distance from cameras to target) is approximately 40cm. The cameras are equipped with Scheimpflug adaptors, a device which is used to tilt the lens relative to the image plane so as to achieve a sharp image across the entire field of view. Each adaptor was connected to a Nikkor 105mm lens, whose aperture varied from f/8 to f/5.6 as the

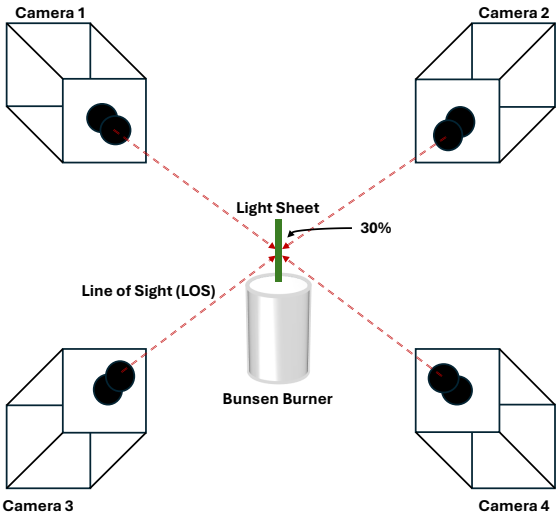

Figure 3.3: 4 cameras pointed towards the target area in a rectangular tomographic orientation. Cameras are placed in a rectangular configuration around the flame at the stand-off distance. The light sheet (green) is also shown illuminating the flame.

light sheet thickness was changed in the different experiments. The lenses and Scheimpflug adaptors were adjusted until all of the particles in the image plane were in focus. The magnification was approximately M = 0.22 for all cameras and the larger field of view used in the majority of the experiments was set to 37mm x 74mm which was imaged onto 1008x2016 sensor pixels. Using equation 3.1 and the information provided above, the depth of field (DOF) was set to approximately 7mm and 3mm for the experiments.

$$DOF = 4.88 f_{\#}^2 W \left(\frac{M+1}{M} \right)^2, \tag{3.1}$$

where $f_{\#}$ is the f-stop of the lenses, W is the wavelength of the laser and M the magnification of an image. The particles were illuminated by a dual cavity 27mJ pulse Nd:YLF laser in a 7mm or 3mm thick light sheet depending on the experiment. The light sheet thickness was controlled by an optical arrangement seen in figure 3.4. Moving from right to left, the first two lenses, one convex (1) and one concave (2), shaped the laser into a beam of slightly more than the required width. An aperture stop (3) was then used to shape the beam exactly to the necessary width by removing the edges of the inherently Gaussian beam. A cylindrical lens (4) was then used to expand the beam in the vertical direction and thus formed a light sheet of approximately 5cm height at the burner exit so that a vertical portion of the flame could be illuminated. Finally, a cut off (5) was placed at the end of the arrangement such that only particles above the burner rim are illuminated and to prevent the laser beam from impinging on the rim of the burner tube and affecting the measurement.

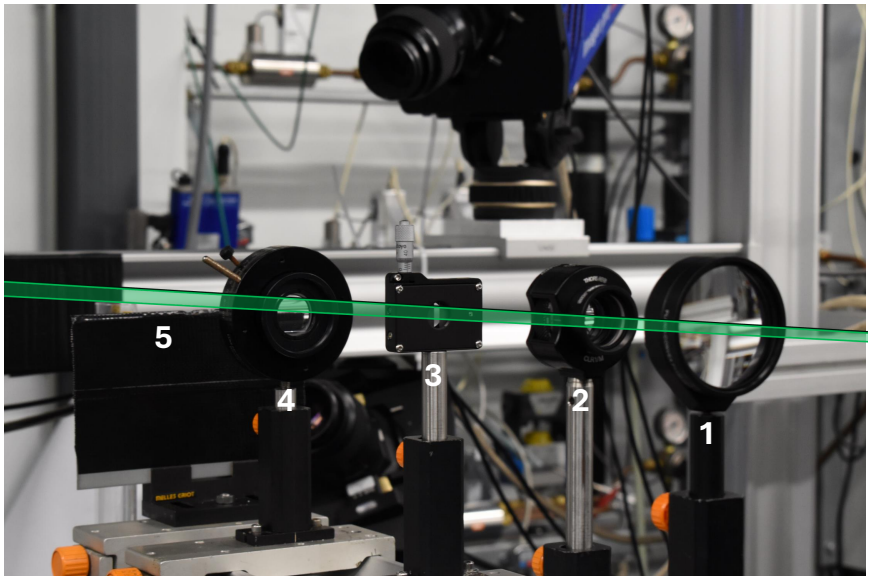

Figure 3.4: Equipment used to shape the beam. The convex lens (1) and concave lens (2) are used to create a beam of constant thickness. An aperture stop (3) fixes the width of the laser beam. A cylindrical lens (4) increases the size of the beam in the horizontal direction and finally the cut-off (5) stops particles below the rim of the tube being studied.

The cameras were synced to the laser system by a programmable timing unit (PTU) which was all controlled from the Davis platform at the main workstation. The varying experiment conditions (table 3.2) resulted in varying timing settings being tested. These are illustrated in figure 3.5. The image acquisition frequency (f) and image time separation (Δt) were varied between experiments.

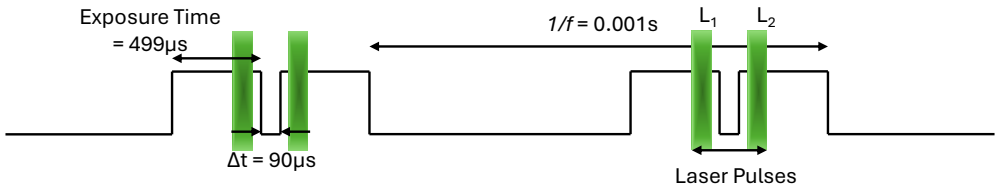

Figure 3.5: Timing diagram example from a sample experiment. The exposure time is the amount of time the camera captures light per image, the time separation Δt (s) is the amount of time between exposures and the amount of time between image pairs is the inverse of the frequency $1/f$. The laser light is pulsed with the camera exposures and its rough timing is illustrated as green pulses.

3.2.1. Image Processing

Before the actual experiment began, all cameras recorded dark images so as to set the zero intensity level correctly. Then once raw images were recorded, they were passed through a sliding minimum filter of 9x9 pixels to remove the background intensity from the images so that only the particle image intensity remained. This is a critical step in obtaining an accurate tomographic reconstruction of the 3D particle distribution. The filter, like most elements of the experiment, is optimised for the data within the unburnt region where the data is more dense and sensitive to change.

These images were then used to complete a volume self-calibration. Initially during an experiment a calibration target is placed in the field of view of all cameras and images are taken to calibrate the cameras to the target. The accuracy of the calibration is enhanced in a second step, known as self-calibration, where particles are identified by triangulation in sub-volumes and incremental corrections are made to the mapping function until high levels of accuracy are achieved (Wieneke, 2008).

A tomographic reconstruction of a subset of the recorded images is then completed with the new calibration. The MART reconstruction method is used with 5 iterations and the resulting projections can be studied to more precisely locate the laser light sheet in the volume. This method of self-calibration

and reconstruction is iterated until the desired volume has been calibrated to within 0.3 pixel in every sub-volume. A complete reconstruction and cross correlation is then completed. The area of reconstitution was approximately 1200x1200x90 voxels^3 or 45x45x3mm^3 in every experiment. The cross correlation is done in 4 steps of 2 passes each with the 75% overlap between neighbouring windows. The linear window size is decreased steadily from 80 voxels to 20 voxels and minimal binning is used, the full settings are displayed in table 3.1. The resulting final window size is 20 voxels^3.

Step	Passes	Size (voxels)	Overlap (%)	Search Radius (voxels)	Binning (voxels)
1	2	80	75	20	2x2x2
2	2	40	75	8	2x2x2
3	2	32	75	4	None
4	2	20	75	2	None

Table 3.1: Settings used in the tomographic reconstruction and further velocimetry cross-correlation.

Finally, the velocity vectors are analysed for outliers. This is shown in figure 3.6. The universal outlier detection method used was proposed by (Westerweel and Scarano, 2005) and detects spurious PIV data. It works by normalising the median residual with respect to an estimate of the local velocity variation within a set range. The neighbourhood of examination was set as 5x5x5 vectors, the threshold was 2 and epsilon 0.25 voxels. The data that was found as an outlier was filled by a smoothing function from the surrounding 5x5x5 window. Once the vector fields were finalised they were exported for examination and post processing. In the image on the left the vectors that are deemed to be outliers by the algorithm (Westerweel and Scarano, 2005) are highlighted in green. On the right the vector field after removing the outliers and applying Gaussian smoothing to the local neighbourhood.

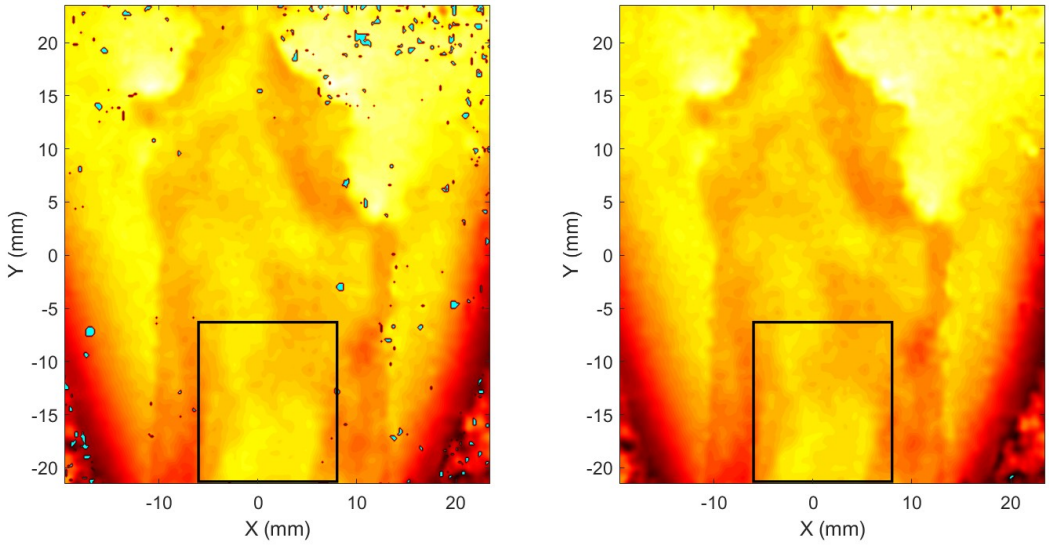

Figure 3.6: Figure highlighting spurious vector detection. On the left, the vectors which have been detected as spurious are shown in light green. On the right, the smoothened version where vectors have been interpolated and replaced. The black box in the figure shows the area used to study the divergence.

3.3. Experimental Methodology

Five sets of experiments were completed for this thesis as can be seen in table 3.2. All experiments were conducted using the same methodology but with varying conditions. One of the objectives of the project was to test if tomographic PIV could be conducted on a standard Bunsen burner flame. Once it was established that this was possible an experiment list was drawn up to test various types of flames and measurement settings. Flame fuel flow conditions were kept the same and only varied for

the hydrogen flames due to stability issues. Although each experiment had a different goal, all were conducted under varying seeding levels. This was done for two reasons. Firstly, low levels of seeding were required for volume self-calibration which is an integral part of the image processing method but, to reconstruct a flame front from the recordings, high levels of seeding were also required. Secondly, as discussed earlier, control of the cyclone seeder was not exact. Therefore seeding levels had to be matched by visual inspection and to save time multiple levels of seeding were recorded as opposed to counting particle levels between recordings.

Experiment Number	Fuel H2 Content (%)	Image Freq f (kHz)	Time Separation Δt (µm)	Light Sheet Depth (mm)	Image/Camera Resolution (pix)
1	0	0.2, 1	90	7	Large (1008x2016)
2	0	4.1	90	7	Small (864x600)
3	0	0.2, 1	90	3	Large (1008x2016)
4	0	1	135, 157.5, 180	3	Large (1008x2016)
5	100	1	30, 45	3	Large (1008x2016)

Table 3.2: Table of Experimental Cases. Each case contains individual experiments as further detailed in the following tables.

Every experiment was conducted using the same experimental setup as discussed in section 3.1. Using the inner diameter of the quartz glass pipe (d = 26mm), the density and the dynamic viscosity of the mixture and a target Reynolds number the required bulk flow velocity could be easily calculated from $u = \frac{Re*\mu}{\rho*d}$. As experiments were all conducted at Reynolds numbers of 4000 or above, the flow is assumed to be a fully developed turbulent pipe flow.

Experiment 1

The first experiment was conducted using a thicker light sheet of 7mm, the experiment conditions are listed in table 3.3. The flame conditions were chosen as they are commonly studied flames and results could be compared to others (Altenburg et al., 2025) and used in future works. The goal of the experiment was to validate if the full depth of the flame produced by the Bunsen burner could be studied with such a depth of field. Images were captured at two frequencies, 1kHz to resolve phenomena at the flame front and front behaviour, and 0.2kHz to compute properties of the flame in a statistically independent manner. Seeding levels were also varied across the recordings.

Runs	Bulk Velocity ($m\,s^{-1}$)	Re	ϕ	Time Separation Δt (µm)	Image Freq f (kHz)	f-stop	Seeding Density
1, 5	2.53	4000	1	125	0.2, 1	8	Medium
2-4, 10	3.48	5500	1	90	0.2	8	Low, High
6-9	3.48	5500	1	90	1	8	Low, Medium, High

Table 3.3: Conditions of Experiment 1.

Experiment 2

The second experiment was conducted using the same light sheet of 7mm, but using a much smaller investigation area. The goal of the experiment was to use a much smaller portion of the camera sensor in order to increase the image recording rate. Images were captured with a field of view of 32mm x 22mm and at a higher frequency of 4.1kHz. The smaller field of view was optimised for the fastest image frequency while maintaining a reasonably sized field of view for flame study. A representation of the area is shown in figure 3.7. An area at the side of the flame, as shown in figure 3.7 was chosen to ensure the flame front remained within the image at all times. The area was chosen at the vertical midway point of the flame as to study the area with the strongest light intensity. In this experiment only the flame of Re = 5500, ϕ = 1, Δt = 90µs was studied as this had been determined as the better flame conditions and time separation for a higher resolution recording. The seeding levels were again varied across the recordings.

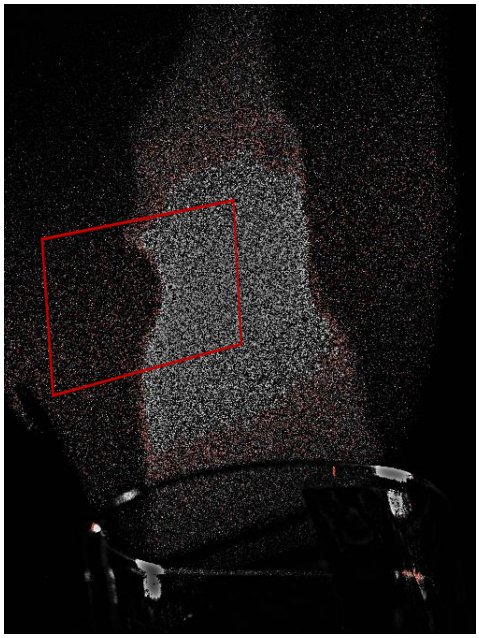

Figure 3.7: A single unprocessed seeded flame image from an individual camera. The red box indicates the studied area in the higher speed experimental run.

Experiment 3

In the third experiment the thickness of the light sheet was decreased to 3mm, as the intensity values of the first two experiments had been deemed as not optimal. This was done for two reasons. Firstly, thinner volumes allow for higher seeding densities for a given reconstruction accuracy (Elsinga et al., 2011), which is beneficial for detection as it creates a larger particle differential across the flame front. Secondly, a thinner volume allows a smaller lens aperture to be used (as seen in equation 3.1 increasing the $f_{\#}$ will result in an increased DOF), which increases the signal-to-noise ratio in the images. Consequently, the f-stop was reduced to 5.6 in the experiment. The full depth of the flame produced was again studied, the experiment conditions used are listed in table 3.4. The goal of the experiment was to validate if a full 3D model of a flame could be studied at the new depth of field. Images were again captured at two frequencies, 1kHz and 0.2kHz. More focus was put on collecting data with varying seeding levels so all levels could be tested in later stages.

Runs	Bulk Velocity ($m\,s^{-1}$)	Re	ϕ	Time Separation Δt (µs)	Image Freq f (kHz)	f-stop	Seeding Density
1-4	3.43	5500	1	90	0.2	5.6	Low, Medium, High
5-8	3.43	5500	1	90	1	5.6	Low, Medium, High

Table 3.4: Conditions of Experiment 3.

Experiment 4

The fourth experiment was again conducted at the reduced 3mm light sheet thickness. The experiment conditions used are listed in table 3.5. The goal of the experiment was to test varying time separation (Δt), as the shift between the particles images was not as high as it should be. A larger particle shift is particularly useful for two reasons. Firstly, it enlarges the jump across the flame front making it clearer to differentiate the burnt and unburnt regions. Secondly, it increases the signal-to-noise ratio in the measured velocity, as the noise level is independent of Δt. Images were only captured at one frequency, 1kHz as statistically independent data could be reasonably achieved by sampling the higher frequency runs. Data was again collected with varying seeding levels so all levels could be tested.

As this experiment produced the most successful results it was the most processed. The final reconstructed volume from an experiment in this run was 1182x1236x95 voxels^3 or 44x46x3.5mm^3.

This results in a voxel size of approximately 0.037mm or 37µm and with a final cross-correlation size of 20 voxels the spatial resolution of the tomographic PIV experiment was determined to be 0.74mm.

Runs	Bulk Velocity ($m\,s^{-1}$)	Re	ϕ	Time Sep Δt (µs)	Image Freq f (kHz)	f-stop	Seeding Density
1-3, 8	3.34	5500	1	135	1	5.6	Low, Medium, High
4-5, 9	3.34	5500	1	157.5	1	5.6	Medium, High
6-7, 10	3.34	5500	1	180	1	5.6	Medium, High

Table 3.5: Conditions of Experiment 4.

Experiment 5

The final experiment was conducted on a Hydrogen flame at the reduced 3mm light sheet thickness. The experiment conditions are listed in table 3.6. The goal of the experiment was to test if the reconstruction could be performed and flame front visualised for a Hydrogen flame. The Reynolds number had to be increased substantially and equivalence ratio decreased so that a stable flame could be achieved. The time separation (Δt) was decreased accordingly as the higher Reynolds number resulted in much faster flows. Images were again only captured at one frequency and at varying seeding levels for a range of tests.

Runs	Bulk Velocity ($m\,s^{-1}$)	Re	ϕ	Time Sep Δt (µs)	Image Freq f (kHz)	f-stop	Seeding Density
1-6	11.78	16000	0.49	45	1	5.6	Low, Medium, High
7-8	11.78	16000	0.49	30	1	5.6	Low, High

Table 3.6: Conditions of Experiment 5.

4

Results and Discussion

4.1. Processing & Kolmogorov Scales

The experimental campaign was conducted to determine the optimum value for two different parameters. The conditions to be varied in the experiment are laid out in table A.1. Firstly, the seeding level. The seeding level is a key parameter to explore as it affects two key elements of the work, the tomographic reconstruction accuracy and the flame front detection. As the seeding level increases the quality of the tomographic reconstruction will decrease as there are more particles along each line of sight (Elsinga et al., 2006). Alternatively, an increase in seeding level will make it easier to detect the flame front as there is a bigger change in particle density across the front. The other parameter investigated in the experimental campaign was the time separation, Δt. The time separation, Δt as discussed in section 3.2 refers to the difference in time between correlated volumes which give the velocity field. An increase in the time separation will result in an increase in the observed particle displacement of a certain field. This should make the velocity jump over the front easier to distinguish from the measurement noise but, as the particle displacement increases it will become increasingly difficult to correlate volume pairs and measure the displacement.

Seeding Level	Time Separation Δt (µs)	Filter Length (Vectors)
High Seeding	90	2-5
	135	2-5
	157.5	2-5
	180	2-5
Medium Seeding	90	2-5
	135	2-5
	157.5	2-5
	180	2-5
Low Seeding	90	2-5
	135	2-5
	135	2-5

Table 4.1: Test Matrix of experiments conducted under 3mm light sheet thickness, contains runs from experiments 3 and 4 as discussed in section 3.3. Further tests are conducted on the results of these runs to identify the best conditions for further study.

4.1.1. Post Processing

Velocity fields obtained for each time step are extracted from Davis and read into Matlab as visualised by the blue vectors in the top left of figure 4.1. The velocity data is organised into three dimensional arrays for each of the three velocity components, mimicking the shape of the data as it was recorded. The first and last three rows, columns and planes of each set are removed as this data is less reliable,

this is shown by the red box in the first image (top left) of figure 4.1. This poor reliability is due to a number of reasons. First, there is increased tomographic reconstruction noise near the boundaries. Second, the first and last planes of the reconstruction are located outside of the light sheet. Third, the correlation windows overlap the boundaries of the reconstructed volume, which affects the accuracy of the result.

The data is then run through a regression filter (Elsinga et al., 2010). The filter works by fitting a second-order polynomial equation via least squares to each component in a local neighbourhood of the velocity field. The radius of a local neighbourhood is set as the filter length and is a parameter to be investigated in this work. The filter produces the filtered velocity fields (shown overlapping the original velocity field in the top right of figure 4.1), and the velocity gradients for every direction as this is used in the spatial element of the regression. The filtered velocity fields are less reliable at the edges because the filter kernel becomes asymmetric near the edges as there is no data available outside the window. Therefore the data that has been affected by the edges is removed and excluded from the results section. This is illustrated as the red box in the bottom left of figure 4.1. This limits the size of the measurement volume that can be used for further analysis to 41.35mm x 43.40mm x 0.93mm. As shown in section 3.2.1 an area at the exit of the pipe is chosen for the assessment of the study accuracy. This area of the velocity field is shown by the black box in figure 3.6.

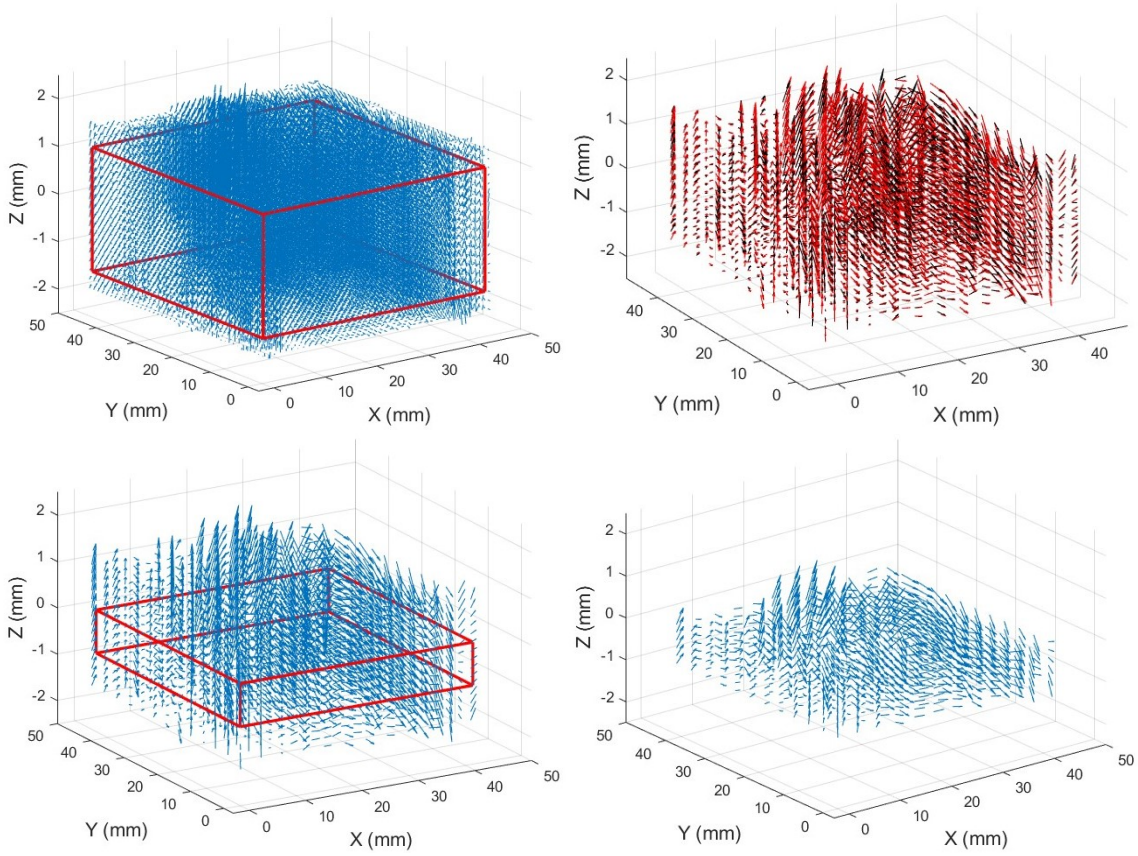

Figure 4.1: The image post processing and filtering displayed in terms of data reduction. In the first image at the top left the full velocity field is shown as exported from Davis in blue containing 247x236x19 vectors, In the second image at the top right the reduced velocity field is shown overlapping with the filtered field of the same size containing 243x232x15 vectors. In the third image at the bottom left the filtered velocity field is shown with the reduced field after removing the edge data in red. The fourth image on the bottom right shows the final velocity field which contains 234x223x6 vectors.

4.1.2. Kolmogorov Scale

As discussed in section 2.1.3 earlier, the Kolmogorov length scale is a scale which represents the smallest scales in a turbulent flow. Here we compare the measurement resolution with the Kolmogorov length scale to understand if the smallest scales and the associated velocity scales have been resolved.

We will examine a point near the exit of the burner tube where the flow can be safely assumed as turbulent pipe flow, a well studied phenomena (White, 2011). For the Reynolds number of 5500 the friction factor of the flow was found to be 0.035 from the Moody diagram. And with a velocity of 3.43m s^{-1} from table 3.4 and a density of 1.16kg m^{-3} this gives a wall shear stress of 0.059 kg m^{-1} s^{-2} and a wall unit of 6.87x10^{-5} m. The Kolmogorov length scale is approximately 3 times the wall unit in core flow region, (Stanislas et al., 2008) and the mean diameters of the core of turbulent vortices is approximately $8 \sim 10$ times the size of Kolmogorov length scale (Ghira et al., 2022). Taking this value as 10, we find a length scale within the flow of 2.07mm, which represents the small-scale structures within the flow. This number also correlates to the physical size of the filter radius 5 which is approximately 1.86mm. As explained in section 3.3 the final spatial resolution of the correlation window was 0.74mm. Therefore, all of the flow should be fully resolved by the measurements. Furthermore, as the area of investigation was 3mm in the third direction it can be assumed there is at least one independent sample of turbulence within the flow.

As tomographic PIV is an experimental technique an accuracy assessment is required to check whether the experiment technique has correctly captured all three velocity components and the overall three dimensional flow. One method used to do this is a divergence check on the velocity gradients of the flow. Divergence is defined as a volume density of flux of a velocity field, and for an incompressible flow mass conservation requires it is zero (Kundu et al., 2016). The region studied is an area downstream of after the exit of the burner and is composed only of the unburnt air and gas mixture which is incompressible and can be assumed to have a uniform temperature.

$$\nabla \cdot \vec{u} = \frac{\partial u}{\partial x} + \frac{\partial v}{\partial y} + \frac{\partial w}{\partial z} = 0 \tag{4.1}$$

In the case that equation 4.1 holds, the sum of any two components of the velocity field should balance with the third. The first term, $\frac{\partial u}{\partial x}$ will be mostly examined as it is in the direction of flow and has the largest velocity component values, it should therefore have the largest velocity gradients. But, the third term, $\frac{\partial w}{\partial z}$ will also be examined as it should highlight the accuracy of the measurement in the third dimension. This is of importance as measuring in the third direction is traditionally difficult and in this case relies on the tomographic reconstruction accuracy.

In the following section figures showing joint pdf's of divergence components are used, figure 4.2 for example. The u component of the divergence is on the horizontal axis and the sum of the v and w components of divergence are on the vertical axis. The contours are in logarithmic scale. The black line indicates zero divergence, i.e. mass conservation. Any deviation of the data from the diagonal indicates measurement error. The further the contours from the line the more error present in the measurement. This is quantified by the standard deviation of the divergence from zero. The datasets studied consist of 20 evenly spaced time steps for each experiment. The amount of data points in each figure ranged from 800,000 to 250,000 depending on the amount of filtering, with the most common filter length of 5 containing 391,680 points.

4.2. Data Selection

In order to understand the potential of the experimental technique for studying turbulent premixed flames the most promising cases are selected. The cases are selected by focusing on three factors. Firstly, we consider the seeding level as this has a large effect on both the tomographic reconstruction and the flame front identification. A lower (0.01 ppp) seeding density traditionally allows for a better reconstruction but makes flame front identification more difficult and a higher seeding density (0.08ppp) offers better flame front identification but decreases the accuracy of the tomographic reconstruction. The next factor is the time separation between images. A larger time shift should result in a greater particle displacement, which in turn reduces the influence of measurement noise (usually a fixed fraction of pixel displacement). However, particle image displacements that are too large can result in significant distortions of the image pattern making correlation more difficult. Finally, the regression filter size is considered. A stronger regression filter requires more data removal from the end result as the data is influenced by points outside the data range, but it offers smoother results. The balance between this noise reduction and the experiments spatial resolution is studied.

4.2.1. Filter Length

The first variable to test for is the filter length used when filtering the raw velocity data. The filter used is a regression filter which uses a method of filtering known as a Savitzky-Golay filtering (Elsinga et al., 2010). The filter works by fitting a second-order polynomial (a quadratic function) to a local 3D region (kernel) of data centred on each vector. The linear size of this region is referred to as the filter length, which represents the number of data points in each direction away from the centre of the kernel or the corresponding physical size in the measurement volume. The quadratic polynomial coefficients are fitted, then from the coefficients we obtain the first derivatives in all three directions (the velocity gradients). The filtering smooths the recorded data but is limited as data close to the edges will be poorly filtered as the function is fitted on an asymmetric kernel.

The dataset chosen to investigate here is from a run with medium seeding and a time separation of 157.5 µs. This data set was chosen as both variables that have been fixed are away from their respective extremes and are less likely to bias the result. The data set is filtered from a neighbourhood radius length of two vectors up to six vectors, six is the maximum as beyond that point there is no remaining data that is not affected by the edges in filtering.

The best cases from this data set are with a filter radius length of four and five. A study of the RMS error on the dimensionless divergence showed decreasing values from a filter radius length of 2 being 1.22 down to a filter radius length of 6 being 0.31. Figure 4.2 shows the divergence plot for filter radius length 4. As can be seen the plot follows the black line from left to right but does show circular behaviour as the left and right sides bulge quite far away from the line.

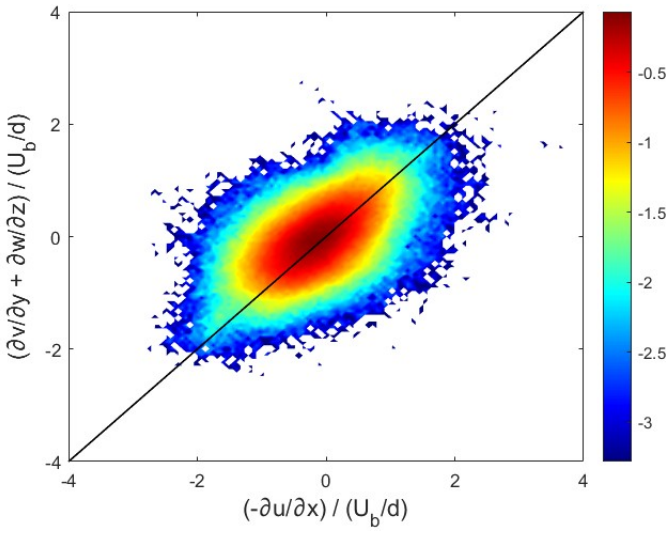

Figure 4.2: Joint pdf of divergence components ($-du/dx$) and ($dv/dy + dw/dz$). The contours are in log scale. The black line indicates zero divergence, any deviation from the diagonal indicates measurement error. The further from the centre line the more error present. Experimental Conditions: Medium seeding ($0.026ppp$), time separation (Δt = 157.5 µs) and a linear filter radius length of 4.

Figure 4.3 shows the divergence plot for the same conditions and a filter radius length of 5. As can be seen the plot follows the zero divergence line much better than the case with filter radius length of 4. This shows a much better filtering of the measurement and matches the window size used in the velocity field post processing previously described. As there is minimal difference in the standard deviation with the filter radius length of 6 and more data is preserved with a filter radius length of 5, the study is continued with a filter radius length of 5.

4.2.2. Time Separation

Using a filter radius length of five the next parameter to investigate is the time separation between the images, as explained in section 3.2.1. To find the best time separation the filter radius length is held constant at five and medium seeding is used as there is good data for all time separations under

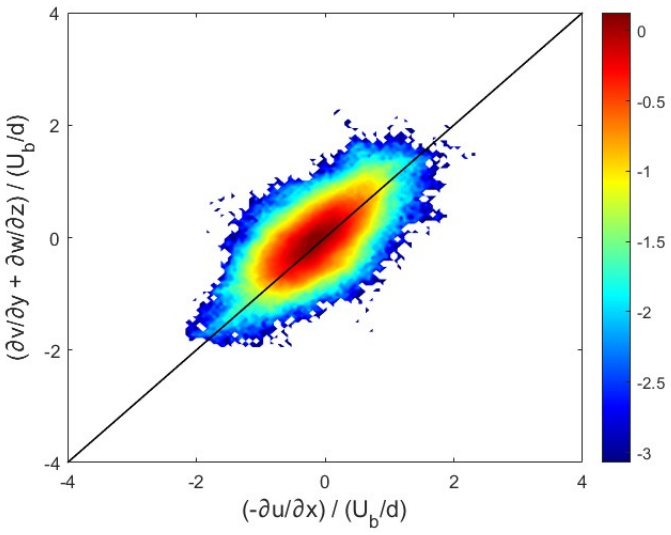

Figure 4.3: Joint pdf of divergence components ($-du/dx$) and ($dv/dy + dw/dz$). The contours are in log scale. The black line indicates zero divergence, any deviation from the diagonal indicates measurement error. The further from the centre line the more error present. Experimental Conditions: Medium seeding ($0.026ppp$), time separation (Δt = 157.5 µs) and a linear filter radius length of 5.

investigation for these conditions. Figure 4.4 shows the divergence plot for a time separation of 135 µs, the plot clearly shows a significant amount of data away from the divergence line in all directions.

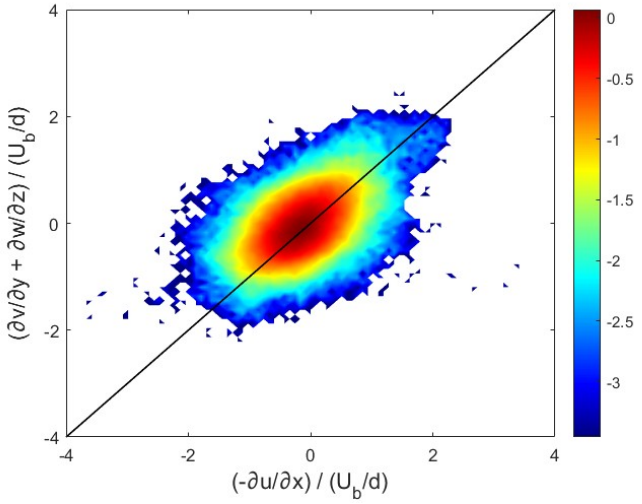

Figure 4.4: Joint pdf of divergence components ($-du/dx$) and ($dv/dy + dw/dz$). The contours are in log scale. The black line indicates zero divergence, any deviation from the diagonal indicates measurement error. The further from the centre line the more error present. Experimental Conditions: Medium seeding ($0.028ppp$), time separation (Δt = 135 µs) and a linear filter radius length of 5.

Figure 4.5 shows the divergence plot for a time separation of 180µs. Here it can be seen that the data follows the line much better. The trend that could be seen in the data was that, as the time step increased from 90µs to 180µs, the RMS error on the dimensionless divergence decreased from 0.68 at 90µs to 0.37 at 180µs. For a time separation of 157.5µs the results also showed a similarly low estimated error of 0.38 and therefore either time separation could be chosen as appropriate. As the estimated error numbers were lower for the highest time separation we will continue using the highest time separation.

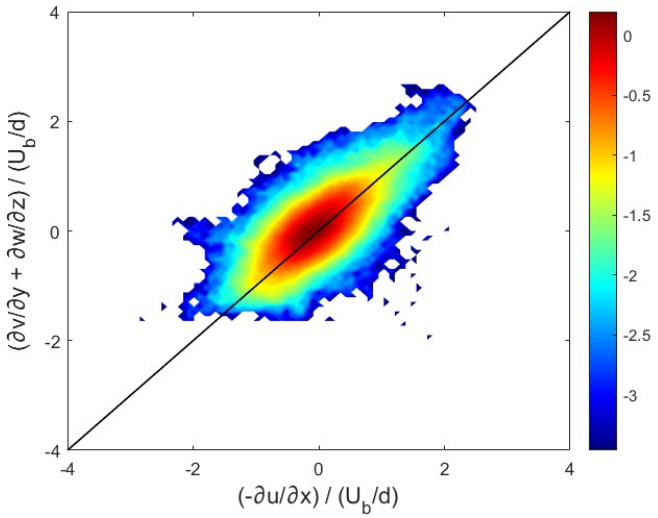

Figure 4.5: Joint pdf of divergence components ($-du/dx$) and ($dv/dy + dw/dz$). The contours are in log scale. The black line indicates zero divergence, any deviation from the diagonal indicates measurement error. The further from the centre line the more error present. Experimental Conditions: Medium seeding ($0.028ppp$), time separation ($\Delta t = 180\mu s$) and a linear filter radius length of 5.

4.2.3. Seeding Level

As the filter radius length has been set at 5 vector spacings ($\sim$ 0.75mm) and the time separation set at Δt = 180µs, the final parameter to be investigated is the seeding density. As described in section 3.1 the seeding was not controlled exactly. This resulted in not all levels of seeding being available at all time separations considered. Seeding levels were estimated by choosing a 20x20pix area of an image in the heavily seeded, unburnt region of the flame and counting the number of prominent particles in the area. This number was then divided by 400 to find the ppp of that run.

As referenced earlier, only medium ($\sim$ 0.03 ppp) and high levels ($\sim$ 0.07 ppp) of seeding were available for higher time separations. As lower seeding densities are generally better for tomographic reconstructions, this is a noted limitation of the experimental study in terms of the measurement

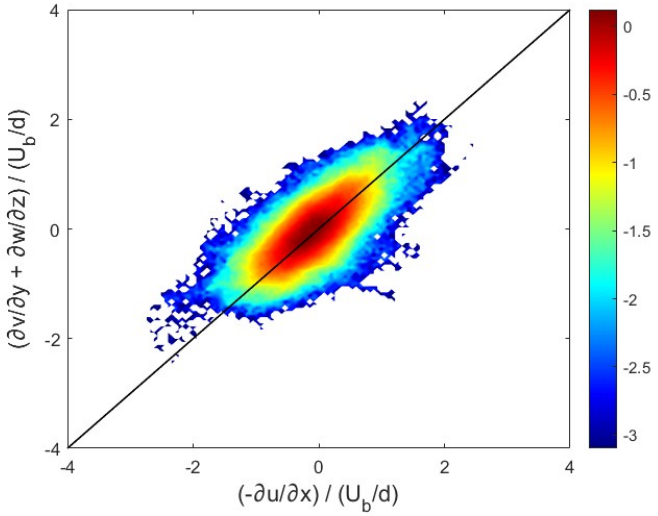

Figure 4.6: Joint pdf of divergence components ($-du/dx$) and ($dv/dy + dw/dz$). The contours are in log scale. The black line indicates zero divergence, any deviation from the diagonal indicates measurement error. The further from the centre line the more error present. Experimental Conditions: High seeding ($0.072ppp$), time separation (Δt = 180µs) and a linear filter radius length of 5.

technique (Scarano, 2012). Although, in order to fulfil the goal of flame front identification and tracking, it will later be shown that high seeding densities are required to effectively achieve this goal. In this section a study of the divergence will verify which measurements are most accurate. These measurements will then be studied again in terms of their capabilities to achieve the experiment goals (i.e. combined flame front velocimetry and tracking).

Figure 4.6 shows the divergence plot for a case of high seeding at 180µs, it can be seen that there is little difference with the previous case of medium seeding (figure 4.5) and the current high seeding at the same time separation. This can also be identified as the standard deviation of the divergence for the high seeding in figure 4.6 (0.35) is very similar to that of the medium seeding in figure 4.5 (0.37). Furthermore, at the slightly lower time separation of 157.5µs there is little difference between the medium and high seeding with both having the same estimated error of 0.38.

In order to further investigate which seeding level is most appropriate, another method of examining the effectiveness of these cases is used. Studying the divergence with the third (z) direction velocity gradient on the horizontal axis of the divergence plot. In tomographic PIV measuring velocity in the depth direction is the least accurate. Plotting with this method should show more visible differences between cases, as this component is better isolated. Examining the four best cases so far; medium and high seeding at both 157.5µs and 180µs very little difference can be found. The cases at 180µs have slightly lower deviations from the divergence line. As can be seen in figure 4.7 the divergence plot highlighting the w component of the velocity gradient on the x-axis has a stronger bulge around 0 on the y-axis as the other components of the velocity field are generally larger.

From this analysis it can be said that the cases which show the most promising results come at high seeding ($\sim$ 0.07 ppp), high time separations (Δt = 180µs) and a filter radius length of five.

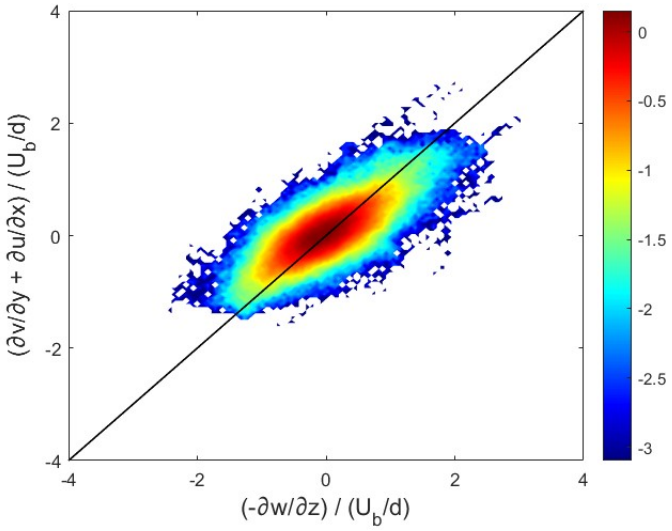

Figure 4.7: Joint pdf of divergence components ($-dw/dz$) and ($dv/dy + du/dx$). The contours are in log scale. The black line indicates zero divergence, any deviation from the diagonal indicates measurement error. The further from the centre line the more error present. Experimental Conditions: High seeding ($0.072ppp$), time separation (Δt = 180 µs) and a linear filter radius length of 5.

4.3. Flame Front

4.3.1. Identification

As explained in section 2.3 the flame front is identified by separating unburnt and burnt flame regions via the number of particles in a certain window. In order for this method to be successful there must be a noticeable difference between the two regions consistently around the flame edge.

Figure 4.8 shows the counts for a highly seeded run. As can be seen the centre of the unburnt region where the light is strongest is very well seeded with over 120 particles in a window. Importantly,

this continues along the edges of the flame front where the majority of the edge windows contain more than 70 particles and the number in the burnt regions is clearly much lower ($\sim$ 30 particles per window). The particle threshold used for highly seeded runs is 42 particles per window.

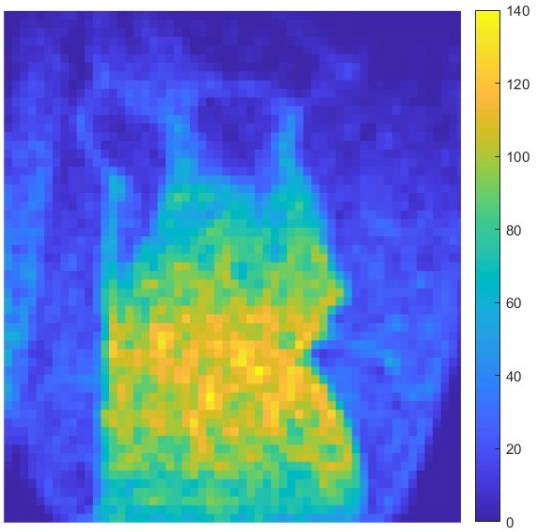

Figure 4.8: The particle count per window for a highly seeded run ($0.072ppp$). Threshold used here is 42.

Figure 4.9 shows the particle counts for a medium seeded run. It can again be seen around the edges of the majority of the flame there is a discernable difference in the number of particles found in a window. The top of the flame front is less clear as the light weakens less particles are imaged by the cameras although they are most likely physically present. The particle threshold used for medium seeded runs is 22 particles per window.

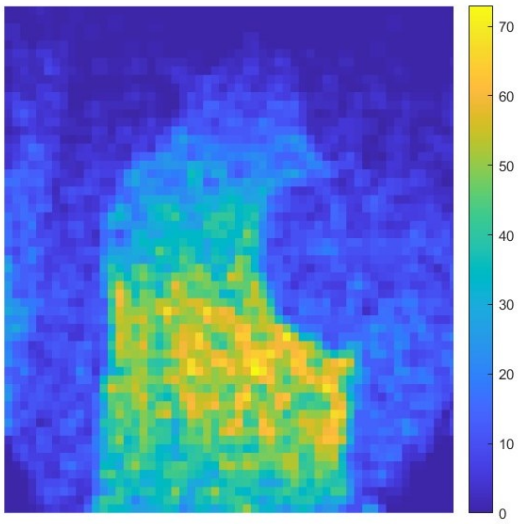

Figure 4.9: The particle count per window for a medium seeded run ($0.028ppp$). Threshold used here is 22.

At low seeding density (figure 4.10) the particle difference at the edges of the flame becomes more difficult to identify. In the centre of the image where the light is the strongest there remains a difference but as we move towards the top and bottom of the flame it becomes impossible to clearly define a flame front. Varying thresholds from 6 to 12 have been tested for this level of seeding but it is not possible to consistently identify a flame front. The lower thresholds will often find shapes that are inconsistent and unphysical and the higher thresholds mostly leave large gaps at certain edges.

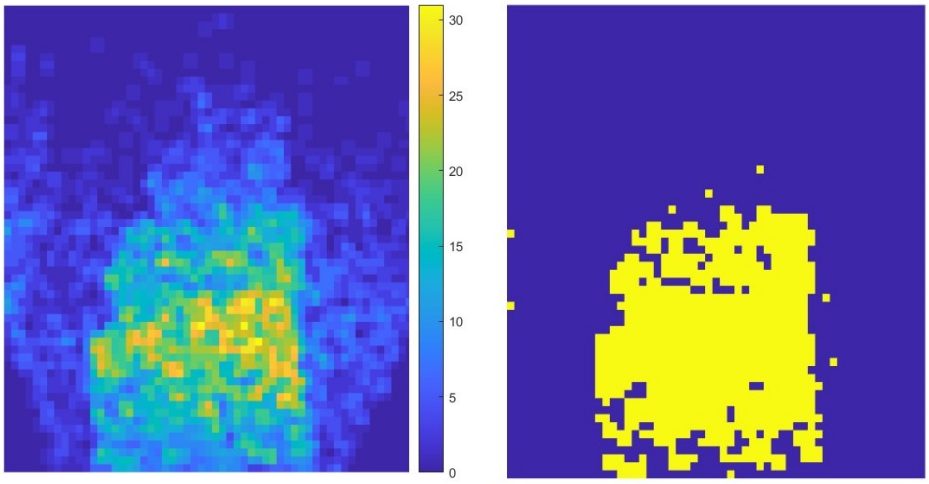

Figure 4.10: Comparison of the particle count per window and binary filter of a low seeded run ($0.012ppp$). On the left, the particle counts is shown, the threshold used on this level of seeding varied from 6-12. On the right, the binary filter for a threshold of 10.

A comparison in the particles per window can be made to figure 2.9, which shows the same process for a highly seeded case. The full flame front is easily identified in the high seeding density cases, particularly without the large gaps that can be seen at the top and bottom of the flame here.

4.3.2. Shifting

There are two methods to examine the shift in the flame front. As described previously using figure 3.5 images are taken in pairs which are separated by the time separation (Δt). Each pair of images is then separated by the inverse of the recording frequency ($\frac{1}{f}$). As the time separation in these experiments is quite short the change in flame front may be too small in some instances to measure the burning velocity. In this situation another possibility is to use the first image from two different image pairs as these are separated by larger time gaps. The recording frequency is also a known value. In the following section each time separation studied in the experiments (table 3.2) will be examined to find appropriately separated fronts. The images shown are individual examples chosen to best represent the findings from large datasets.

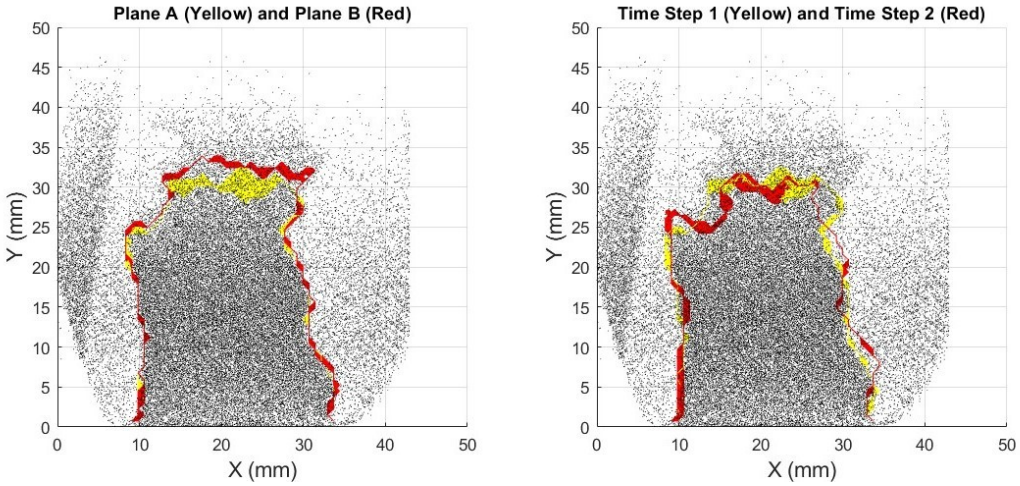

Figure 4.11: On the left, the shift in flame front from the time separation of 90µs. The first image of the pair is the yellow the second the red. On the right, the shift from the first time step of two image pairs separated by the image frequency (1000µs). The image from the first pair is in yellow and from the second in red. The grey dots are the particle reconstruction from the first image of the first pair, the highly seeded area on the left is reconstruction noise. It can be seen the larger image frequency difference produces a more substantial shift. The run is highly seeded ($0.056ppp$).

First, figure 4.11 (left) shows the smallest time separation of 90µs. The image shows two flame fronts which are separated by the time separation, as can be seen the flame fronts are mostly overlapping in all side areas. The area at the top of the flame doesn't overlap as well but this area is not reliable. Particle imaging is much more difficult at the top of the image due to low intensity light. Any variation in the light intensity (between the two pulses) may result in a shift in detected flame front that is not physical. The image on the right shows two flame fronts which are separated by the image time step. This image shows more separation and variation in the side regions of the flame. It is clear from these images that the image frequency would be more effective in order to track flame front motion.

Next, figure 4.12 shows the higher time separation of 157.5µs. The other middle time separation of 135µs is skipped as its results are mostly similar to this time separation. Again, on the left side the flame fronts are separated by the time separation and on the right side the flame fronts which are separated by the image time step. In this set of images the fronts are mostly overlapping everywhere, this was generally the case throughout the data. On some occasions a discernable difference could be found in certain features of flames as seen on the right side of the right image but in general this time separation is not very suited to burning velocity calculations and the image frequency is still more effective.

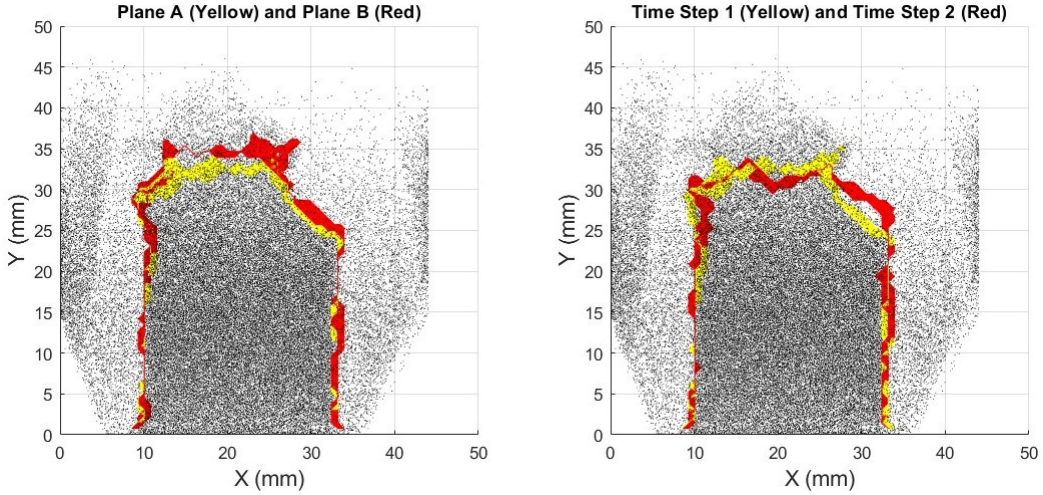

Figure 4.12: Images displaying the shift in flame front. On the left, the shift in flame front from the time separation which for this run is at 157.5µs. On the right, the shift from the first time step of two image pairs separated by the image frequency (1000µs). It can be seen that there is not a large difference between the two methods. The run is highly seeded ($0.078ppp$).

Finally, figure 4.13 shows the highest time separation of 180µs. Again, on the left side fronts separated by the time separation and on the right side fronts separated by the image frequency. The left side shows flame fronts which are mostly overlapping. It can be seen that the red flame front is 'wider' at the top of the flame, this is due to motion in another plane as this is a 2D view of a 3D surface. This effect is more common at the higher time separation value. The right figure shows clear separation in both the top and at the side of the front. A clear shift in the front can be seen from one position to another and in general this image time step is more suited to burning velocity calculations. Although, as will be discussed in section 4.4, the top of the flame front detection is less reliable due to less light being available when compared to the divergence plots. A comparison between these two methods of tracking can be made. Shifts in the tops of flame fronts are considered but activity in the middle portion of the flame front where the light is strongest are given more weight when drawing conclusions about the effectivity of the methods.

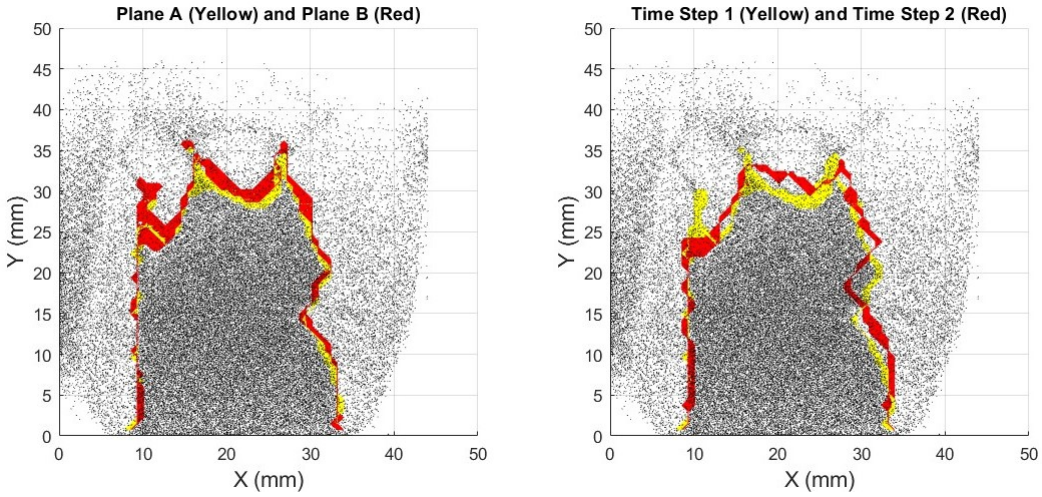

Figure 4.13: Images displaying the shift in flame front. On the left, the shift in flame front from the time separation which for this run is at 180μs. On the right, the shift from the first time step of two image pairs separated by the image frequency (1000μs). It can be seen that fronts separated by the image frequency produce a clearer shift in location. The run is highly seeded ($0.072ppp$).

4.3.3. Flame Front Velocities

The first step towards acquiring turbulent burning velocities is measuring the fluid velocity at the flame front. In order to do this the instantaneous velocity fields calculated from the measurements must be matched with the flame front derived previously in this section.

Figure 4.14 shows the particle distribution of a flame, the corresponding flame front surface and finally a sample of velocity vectors in a single image. The flame front surface is made up of many triangles combined together into a single surface. This surface was obtained from the flame front threshold detection as described in section 2.3. The centroid of each triangle is found and the fluid velocity field (obtained by tomographic PIV) is interpolated to find the velocity at that point in three dimensional space. The velocity vector is then plotted with its velocity magnitude corresponding to length of the vector in the plot.

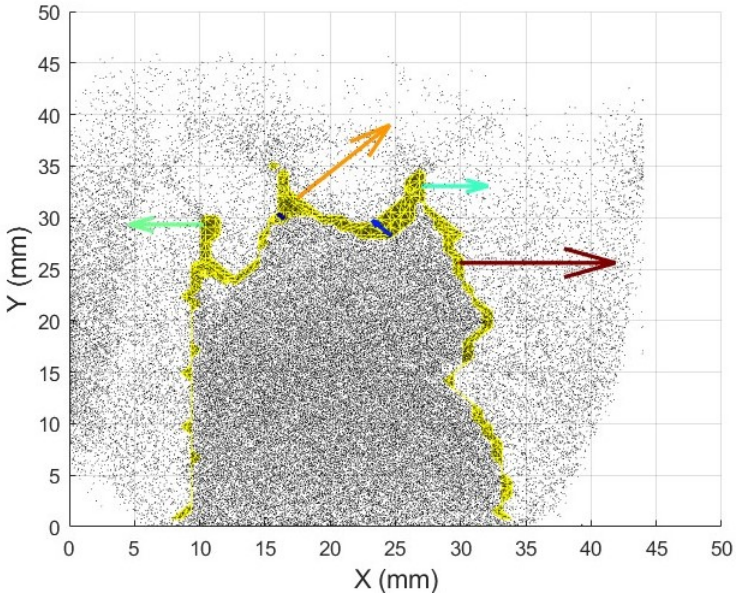

Figure 4.14: Two dimensional view of the flame front, seeding particles and selected flame front velocity vectors. The velocity vectors colour and size indicate their magnitude. The experimental conditions for this run were; High seeding ($0.072ppp$), time separation (Δt = 180μs) and a linear filter radius length of 5.

Figure 4.15 displays the same time instant as in figure 4.14 but in 3D. As it can be seen there are large velocity magnitudes in all three directions. The three arrows on the right are all moving in the same direction indicating the fluids movement.

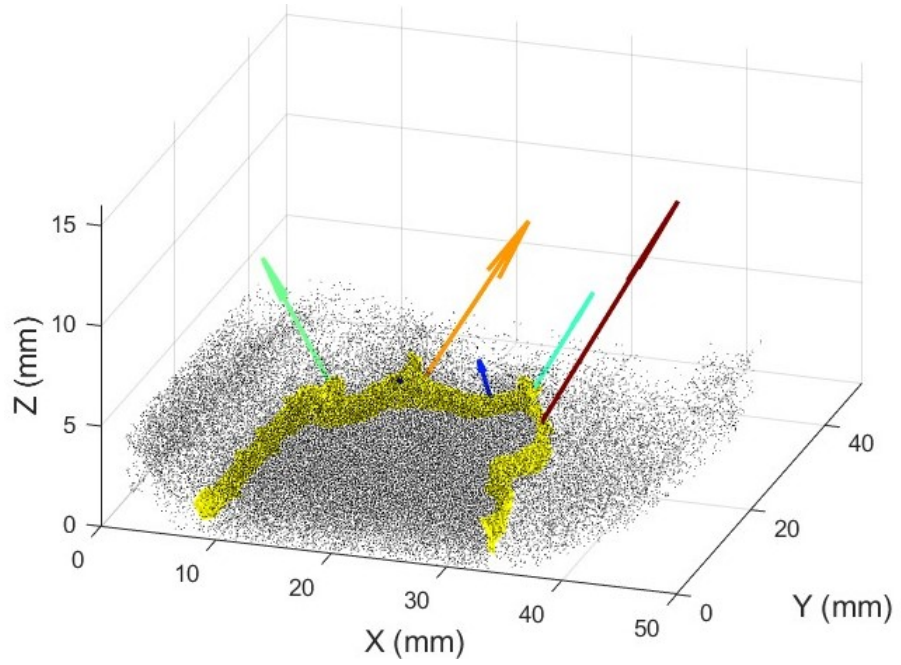

Figure 4.15: Three dimensional view of the flame front, seeding particles and selected flame front velocity vectors. The velocity vectors colour and size indicate their magnitude. The experimental conditions for this run were; High seeding ($0.072ppp$), time separation (Δt = 180μs) and a linear filter radius length of 5.

4.4. Validation of Flame Front Detection

Due to the experimental nature of the work, validation poses an interesting task. One approach follows on from previous studies of divergence. Plotting of the divergence at a certain time should match up with a flame front constructed from the particle number density method at the same time. This occurs as the gas mixture is heated and expands as it crosses the flame front. This expansion causes divergence. Although the location of the highest thermal expansion and largest seeding difference are not proven measures of the exact flame front they are very good approximations and should be similar. Again we will look at our four cases varying in seeding level and time separation to see if one experimental conditions is better than the others.

Figure 4.16 displays a divergence plot in *x* and *y* for a run of medium seeding and a high time separation (180μs). The colours and the corresponding colour scheme on the right represent the divergence level and the black surface is the flame front surface. The yellow divergence level represents where the velocity of the flow is rapidly increasing as per the colour bar at the side of the figure. This can be seen as a version of the flame front. This divergence level shows good overlap with the flame front, except for at the top of the image where particle detection suffers from a less powerful light sheet, leading to a lower particle detection probability and hence lower measured particle concentrations. The two areas at the tip of the flame front which have much higher and lower divergence are vortices forming at the edge of the flame front. The image on the left shows the flame front from the first time step from the correlated pair and the image on the right the second time step from the pair. The divergence is derived from the change between the velocity fields at each of the two time steps over a defined period.

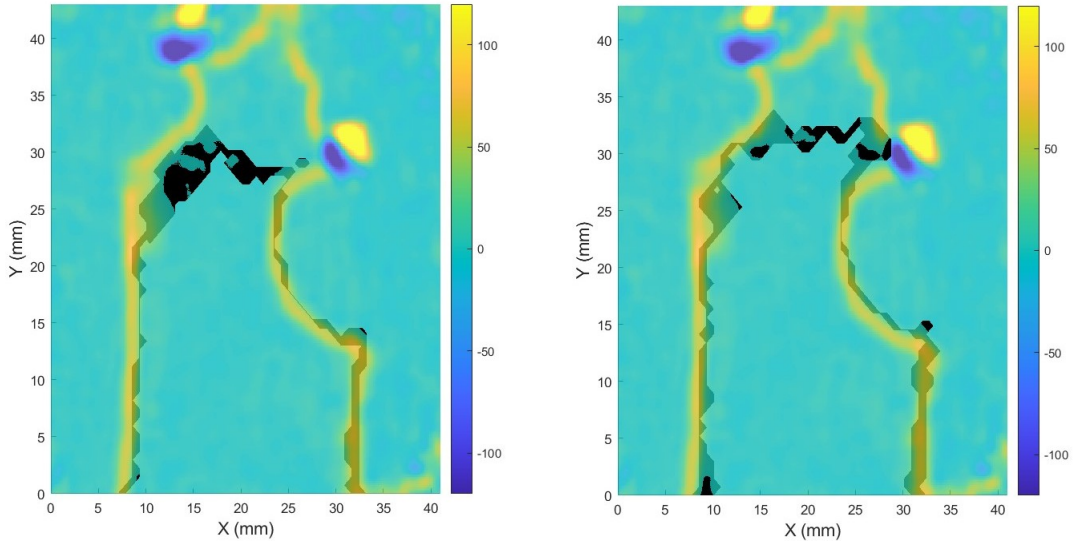

Figure 4.16: Comparison of divergence magnitude and flame front detection from the binary filter. On the left, the image shows the first plane and on the right, the second plane of a single time step. Divergence is calculated from the change in the velocity fields at the two instances, and is therefore the same for both flame fronts. This example shows a run with medium seeding (0.028). A time separation of Δt = 180µs and a linear filter radius length of 5 is used to evaluate divergence.

Figure 4.17 shows the flame front and divergence for a run of medium seeding and at a lower time separation of 157.5µs. It can again be seen that the flame front is well matched to the divergence, even though there is much more variance in the shape of this flame front. Again the top of the image shows where the flame front tracking is limited by light. It can also be seen that the movement in the flame front from one time step to another is less as the time separation is smaller.

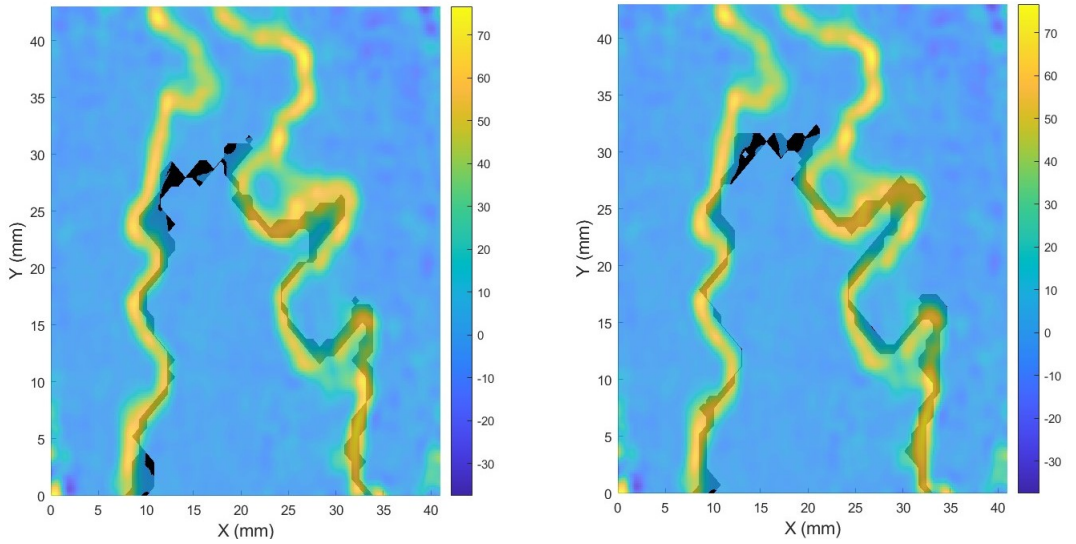

Figure 4.17: Comparison of divergence magnitude and flame front location from the binary filter. On the left, the image shows the first plane and on the right, the second plane of a single time step. Divergence is calculated from the change in the velocity fields at the two instances, and is therefore the same for both flame fronts. This example shows a run with medium seeding (0.026). A time separation of Δt = 157.5µs and a linear filter radius length of 5 is used to evaluate divergence.

Figure 4.18 shows the comparison for a highly seeded run with the same time separation of 157.5µs. In comparison to figure 4.17, there is little to no difference in the matching of flame front to divergence. This finding is the same when comparing to figure 4.16 which has both a higher seeding concentration and a lower time separation.

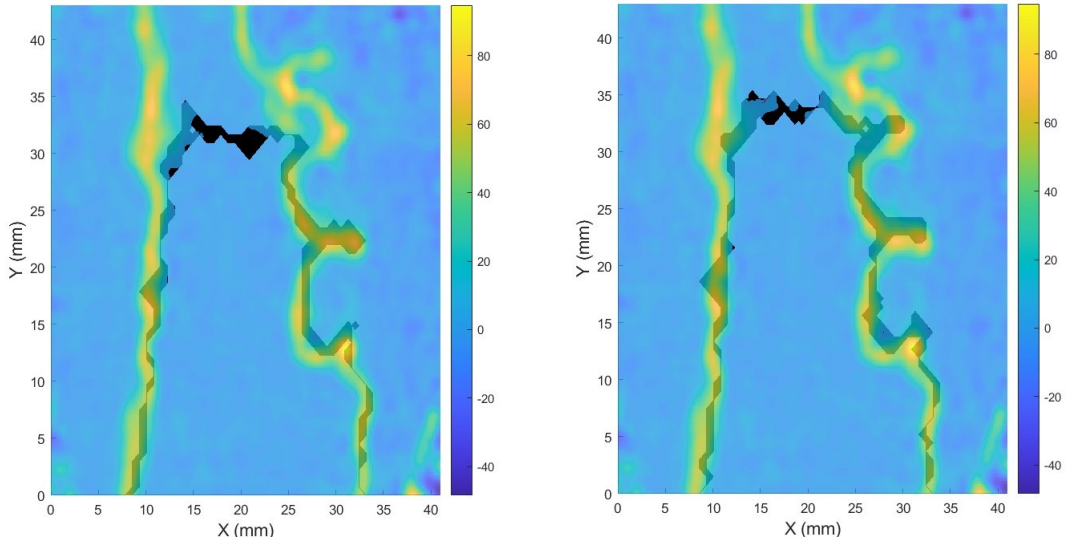

Figure 4.18: Comparison of divergence magnitude and flame front location from the binary filter. On the left, the image shows the first plane and on the right, the second plane of a single time step. Divergence is calculated from the change in the velocity fields at the two instances, and is therefore the same for both flame fronts. This example shows a run with high seeding (0.078). A time separation of Δt = 157.5µs and a linear filter radius length of 5 is used to evaluate divergence.

Figure 4.19 shows the comparison for a highly seeded run with the high time separation of 180µs. This run shows mostly similar behaviour to the other settings but struggles sometimes to identify the front well. This is best seen at the right side of the figures where the front does not always match-up with the divergence plot. This behaviour can be seen often in the data for runs with the highest seeding and highest time separation. For these settings it can be seen visually in the recorded seeding images that there are sometimes small bunches of seeding or other types of seeding inconsistencies passing through the flow. This was deemed to be an instance of chance as other runs with similar levels of seeding were not affected by similar conditions. The process of preparing the seeding may not have been as well observed for this experiment.

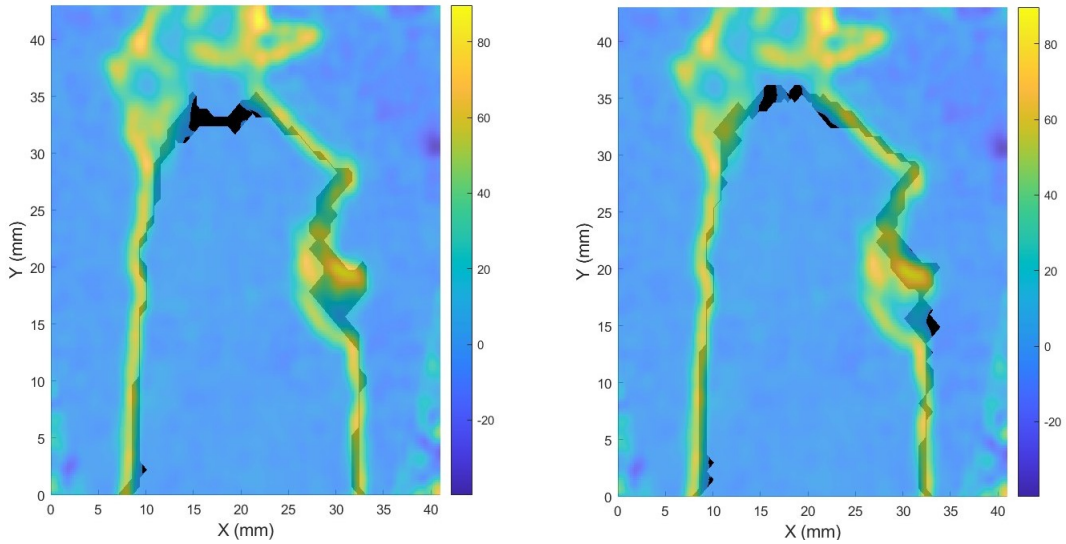

Figure 4.19: Comparison of divergence magnitude and flame front location from the binary filter. On the left, the image shows the first plane and on the right, the second plane of a single time step. Divergence is calculated from the change in the velocity fields at the two instances, and is therefore the same for both flame fronts. This example shows a run with high seeding (0.072).A time separation of Δt = 180µs and a linear filter radius length of 5 is used to evaluate divergence.

Figure 4.20 shows more examples from the same run as in figure 4.19 and highlights further the discrepancies between the flame front and the divergence of the flow at these conditions. In the figure on the right the flame front extends beyond the area where divergence is highest. Upon further

inspection it is hard to visually see why this would occur. It is most likely due to the velocity peaks at the flame front where the gas is sped up, this can result in more interpolated vectors and a slightly less accurate divergence peak on the diagram.

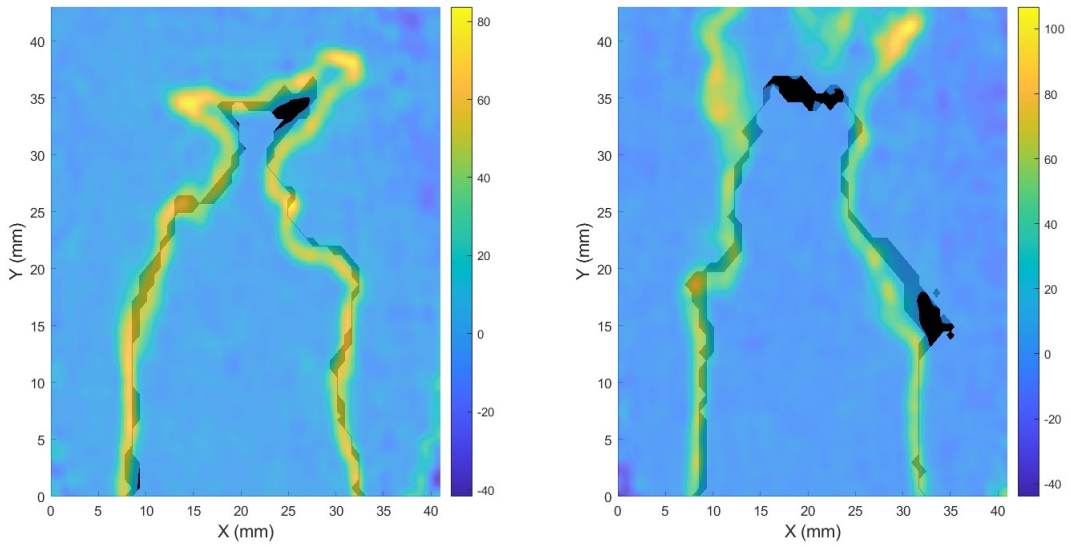

Figure 4.20: Comparison of divergence magnitude and flame front location from the binary filter. On the left, the image shows the first plane and on the right, the second plane of a single time step. Divergence is calculated from the change in the velocity fields at the two instances, and is therefore the same for both flame fronts. This example shows a run with high seeding (0.072). A time separation of Δt = 180µs and a linear filter radius length of 5 is used to evaluate divergence.

4.5. Error Propagation

The uncertainty on the velocity can be estimated by looking at the uncertainty on the velocity gradient. The standard deviation of the non-dimensionalised divergence is approximately 0.35 on the best runs, as found earlier. The divergence was non-dimensionalised by dividing it by 130.77s^{-1}, which is the characteristic velocity of the flow, 3.4m s^{-1} divided by the characteristic length scale 0.026m. So converting the standard deviation of the non-dimensionalised divergence to dimensional units gives a standard deviation of 45.77s^{-1}. As the area that is studied is incompressible then the standard deviation can be assumed to be the uncertainty on the divergence at a 68% confidence level. Assuming that the error on each of the three velocity components is equal, the uncertainty on a single velocity gradient can then be computed as $\frac{45.77}{\sqrt{3}}$ = 26.43s^{-1}.

The uncertainty of the divergence can furthermore, be related to the uncertainty on the measured velocity. Here, the relation is established using a simulation. First, a random velocity noise field is generated of the same size as the original field (247x236x19 grid). Maximum and minimum values for the field are set to resemble the magnitude of the true velocity field. Then a 5x5x5 smoothing is applied to include the effect of the PIV cross-correlation windows and 75% overlap. The noise PIV velocity field is then processed in MATLAB as described in section 4.1.1 using a filter kernel of 5x5x5. Using the standard deviation of this filtered velocity field a measure of the uncertainty on the velocity we can compute a relationship between this uncertainty and the uncertainty on the divergence. The sample random PIV velocity field has a standard deviation of 0.107m s^{-1}, the sample divergence field computed from this velocity field has a standard deviation of 35.520s^{-1}. Applying the ratio between the two to the uncertainty on the divergence of the experiment (45.77 s^{-1}), the uncertainty on a single velocity component is found to be 0.14m s^{-1} (prior to smoothing).

In order to examine the statistical convergence of the measurement, the number of independent samples in the experiment can be found and studied. To find the number of independent samples the auto-correlation (R_{xx}) is measured and used to find the auto-correlation coefficient (C_{xx}). The location chosen to study the auto-correlation is at the exit of the pipe in the incompressible region, the time

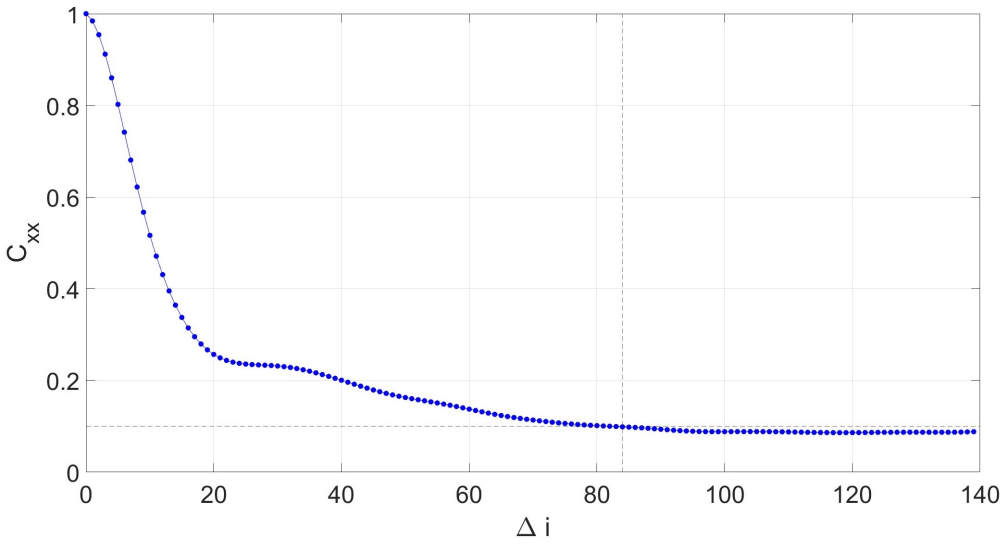

Figure 4.21: On the vertical axis the auto-correlation coefficient of a component of the raw velocity field, on the horizontal axis the number of time steps between measurements. The full sample is comprised of 1000 samples recorded at 1kHz. The threshold is highlighted on the vertical axis and the number of coherent samples on the horizontal. High seeding ($0.072ppp$), time separation (Δt = 180µs) and a linear filter radius length of 5.

series is then run for all samples in the experiment which produced the best results (1000). The auto-correlation coefficient for this experiment is displayed as a function of sampling distance (in time) in figure 4.21. As can be seen for a threshold of 0.1 the number of coherent samples is 84, this results in the number of independent samples N being 74, meaning that there is temporal similarity for 84 samples at a time, this is due to the continuous nature of the flow.

5

Conclusions and Recommendations

5.1. Conclusions

In conclusion a tomographic particle image velocimetry experimental setup has been construed and turbulent premixed natural gas and hydrogen flames studied. Four LaVision Imager Pro HS 4M's were arranged in a rectangular form and focused on the exit of a Bunsen burner tube. A LabView panel was created on the lab computer and connected to mass flow controllers to control the flow of air, natural gas and hydrogen. The gas flows were connected to the Bunsen burner setup and the cameras focused and calibrated to the flow. Five sets of experiments were conducted testing for multiple parameters. In terms of tomography, the depth of field that could be recorded and reconstructed was tested as well as the recording rate (image frequency). Experimental parameters were also optimised during the experiments, the seeding density, image time separation and filter length were all tested at varying conditions.

The primary conclusion from this work is that flame front detection can be accurately conducted alongside tomographic particle image velocimetry. As shown in section 4.2 three dimensional velocity fields of high accuracy can be captured on flames, while section 2.3 discussed how accurate flame fronts were tracked. The main limitation of this combination of techniques is the seeding density, intuitively a lower seeding density (<0.03ppp) is required for accurate tomographic PIV whereas a higher seeding density would allow for more accurate flame front reconstructions. In this work it was found that a minimum seeding density of approximately 0.05ppp is necessary for accurate flame front detection, levels lower than this resulted in a low spread of particles across each window making it difficult to differentiate the flame front with a single threshold. At the higher level of seeding tomographic PIV was found to be successful, by studying an area of theoretically zero divergence pdf's of divergence components could be used to quantify the experiments measurement accuracy. This method indicated that flows with higher levels of filtering and time separation were best and found that higher levels of seeding did not diminish the quality of the measurement, furthermore similar results were found when focusing on the w velocity component indicating accurate three dimensional measurements.

One limiting factor in the experiment was data collection, this was driven by a few factors. Raw velocity fields were post processed using a regression filter which decreased the size of the velocity field due to accuracy around the field edges. Filtering the data was important to the accuracy of the final results and became more important as the seeding density of the experiment was increased. The initial depth of the field which was recorded (7mm) had to be reduced to 3mm in order for the laser to illuminate the entire field of view of every camera. An increased light budget would be required in order to increase this depth of field and therefore the size of the measured three dimensional velocity field. This would result in more raw data and finally more data after filtering and post processing. Another limiting factor of the current experimental setup was found when studying flames with a higher percentage of hydrogen. Increasing the hydrogen percentage in the mixture in the bunsen burner setup required a higher flow velocity to maintain flame stability. To accurately track the flame fronts of these flames cameras with much higher recording rates would be required.

5.2. Recommendations

As the experimental scope must be finite in a busy laboratory and the processing that can be done by a single student is limited, the experiments that were conducted were pre-determined before results could be seen. This meant the focus of the experiment leaned towards natural gas flames where the results were most likely to be promising. The experiments that were run on hydrogen indicated promising results and should be studied further. Figure B.1 shows the joint pdf of divergence components under the same conditions as in the chapter 4.2 of a promising hydrogen flame run. The graph is less populated as the full post processing of the hydrogen runs have not been complete at this time. Further experiments should be run in order to optimise the same experimental conditions for predominantly hydrogen flames as were in this work for predominantly natural gas flames. This work would result in a better understanding of the conditions required to conduct PIV on higher speed hydrogen flames as well as how the differing light conditions from the flame affect flame front detection. Presumably paving the way for successful measurements of flame front velocities.

As was discussed in section 4.3.2 the separation chosen between flame images is crucial to how the flame front velocity is measured. The method used in this work was chosen as it best suited the goal of the experiment from the two options available, an experiment could have also be designed around testing for this variable. Inherently within the experimental setup there is the ability to vary both the time separation of an image pair as well as the acquisition frequency (figure 3.5). This potentially could have resulted in image separations more favourable for flame front velocity calculations. Following on from this there is scope for improvement in the method used to calculate the flame front velocity, as discussed in detail by Driscoll (2008) and Altenburg et al. (2025). Further experiments could be designed around this idea, with the goal of finding an accurate and consistent method to track the flame front velocity in reality.

Another consideration that should be made for studying predominantly hydrogen flames is the image acquisition rate required is much higher than for predominantly natural gas flames. As hydrogen flames propagate and evolve much faster, the turbulent structures within occur on shorter time scales. To combat this cameras with much higher acquisition rates would be required. Other improvements could be made in the lab conditions such as an increase in the light budget for better particle visualisation and a potential increase in the DOF achievable. An increase in the resolution of the cameras sensors for better spatial resolution of the images would also allow for more in-depth study of hydrogen flame structures. Finally, as tomographic PIV is a computationally taxing venture more powerful computing or more efficient algorithms would improve the human time required in the data processing. Large data sets require more human time to process efficiently and put more strain on the universities computational resources.

References

[1] R. Adrian. “Particle-Imaging Techniques for Experimental Fluid Mechanics”. In: *Annual Review of Fluid Mechanics* 23.1 (Jan. 1991), pp. 261–304. DOI: 10.1146/annurev.fl.23.010191.001401.

[2] R. Adrian and J. Westerweel. *Particle image velocimetry*. Cambridge aerospace series 30. Cambridge: Cambridge Univ. Press, 2011.

[3] L. Altenburg, S. Klein, and M. Tummers. “Flame-induced pressure gradients in turbulent premixed natural gas-air and hydrogen-air jet flames”. In: *Combustion and Flame* (2025). [Accepted for Publication].

[4] M. P. Arroyo and C. A. Greated. “Stereoscopic particle image velocimetry”. In: *Measurement Science and Technology* 2.12 (Dec. 1, 1991), pp. 1181–1186. DOI: 10.1088/0957-0233/2/12/012.

[5] C. Atkinson and J. Soria. “An efficient simultaneous reconstruction technique for tomographic particle image velocimetry”. In: *Experiments in Fluids* 47.4 (Oct. 1, 2009), pp. 553–568. DOI: 10.1007/s00348-009-0728-0.

[6] C. Brücker. “Digital-Particle-Image-Velocimetry (DPIV) in a scanning light-sheet: 3D starting flow around a short cylinder”. In: *Experiments in Fluids* 19.4 (Aug. 1995), pp. 255–263. DOI: 10.1007/BF00196474.

[7] B. Coriton, A. Adam, and J. Frank. “High-speed tomographic PIV and OH PLIF measurements in turbulent reactive flows”. In: *Experiments in Fluids* 55.6 (June 3, 2014), p. 1743. DOI: 10.1007/s00348-014-1743-3.

[8] B. Coriton and J. Frank. “High-speed tomographic PIV measurements of strain rate intermittency and clustering in turbulent partially-premixed jet flames”. In: *Proceedings of the Combustion Institute* 35.2 (2015), pp. 1243–1250. DOI: 10.1016/j.proci.2014.06.045.

[9] G. Damköhler. “Der Einfluss der Turbulenz auf die Flammengeschwindigkeit in Gasgemischen”. In: *Zeitschrift für Elektrochemie und angewandte physikalische Chemie* 46.11 (Nov. 1940), pp. 601–626. DOI: 10.1002/bbpc.19400461102.

[10] J. Driscoll. “Turbulent premixed combustion: Flamelet structure and its effect on turbulent burning velocities”. In: *Progress in Energy and Combustion Science* 34.1 (Feb. 2008), pp. 91–134. DOI: 10.1016/j.pecs.2007.04.002.

[11] D. Ebi and N. T. Clemens. “Simultaneous high-speed 3D flame front detection and tomographic PIV”. In: *Measurement Science and Technology* 27.3 (Mar. 1, 2016), p. 035303. DOI: 10.1088/0957-0233/27/3/035303.

[12] T. Echekki and E. Mastorakos. *Turbulent Combustion Modeling: Advances, New Trends and Perspectives*. Vol. 95. Fluid Mechanics and Its Applications. Springer, Netherlands, 2011. DOI: 10.1007/978-94-007-0412-1.

[13] G. Elsinga, R. J. Adrian, B. W. Van Oudheusden, and F. Scarano. “Three-dimensional vortex organization in a high-Reynolds-number supersonic turbulent boundary layer”. In: *Journal of Fluid Mechanics* 644 (Feb. 10, 2010), pp. 35–60. DOI: 10.1017/S0022112009992047.

[14] G. Elsinga, F. Scarano, B. Wieneke, and B. W. van Oudheusden. “Tomographic particle image velocimetry”. In: *Experiments in Fluids* 41.6 (Dec. 1, 2006), pp. 933–947. DOI: 10.1007/s00348-006-0212-z.

[15] G. Elsinga, J. Westerweel, F. Scarano, and M. Novara. “On the velocity of ghost particles and the bias errors in Tomographic-PIV”. In: *Experiments in Fluids* 50.4 (Apr. 1, 2011), pp. 825–838. DOI: 10.1007/s00348-010-0930-0.

[16] European Commission. *GHG emissions of all world countries :2023.* Italy: Joint Research Centre, Publications Office, 2023.

[17] F. Faldella. *Experimental Investigation of Boundary Layer Flashback in high H2 Concentration Turbulent Premixed Jet Flames*. Technische Universiteit Delft, Apr. 17, 2020.

[18] B. Fine. *Further experiments on the stability of laminar and turbulent hydrogen-air flames at reduced pressures*. Technical Report NACA-TN-3977. Clevehand, Ohio: Lewis Flight Propulsion Laboratory, Apr. 1, 1957, pp. 1–32.

[19] S. Fu, P. H. Biwole, and C. Mathis. "Numerical and experimental comparison of 3D Particle Tracking Velocimetry (PTV) and Particle Image Velocimetry (PIV) accuracy for indoor airflow study". In: *Building and Environment* 100 (2016), pp. 40–49. DOI: https://doi.org/10.1016/j.buildenv.2016.02.002.

[20] A. A. Ghira, G. E. Elsinga, and C. B. da Silva. "Characteristics of the intense vorticity structures in isotropic turbulence at high Reynolds numbers". In: *Physical Review Fluids* 7.10 (Oct. 14, 2022). Publisher: American Physical Society, p. 104605. DOI: 10.1103/PhysRevFluids.7.104605.

[21] D. Gragg. "Energy for Transportation". Stanford, Oct. 25, 2023.

[22] K D Hinsch. "Holographic particle image velocimetry". In: *Measurement Science and Technology* 13.7 (July 1, 2002), R61–R72. DOI: 10.1088/0957-0233/13/7/201.

[23] M. J. Hurley, G. Jomaas, D. Gottuk, J. R. Hall, K. Harada, E. Kuligowski, M. Puchovsky, J. Torero, J. M. Watts, and C. Wieczorek. "Fundamentals of Premixed Flames". In: *SFPE Handbook of Fire Protection Engineering*. 5th ed. Vol. 1. Springer, New York, 2016, pp. 373–395. DOI: 10.1007/978-1-4939-2565-0_12.

[24] IEA. *CO2 Emissions in 2023*. Paris: IEA, 2024.

[25] P. K. Kundu, I. M. Cohen, D. R. Dowling, and G. Tryggvason. *Fluid mechanics*. Sixth edition. Amsterdam ; Boston: Elsevier/AP, 2016. 921 pp.

[26] C. K. Law. *Combustion Physics*. 1st ed. Cambridge University Press, New York, Sept. 11, 2006. DOI: 10.1017/CBO9780511754517.

[27] J. M. Lawson and J. R. Dawson. "A scanning PIV method for fine-scale turbulence measurements". In: *Experiments in Fluids* 55.12 (Nov. 19, 2014), p. 1857. DOI: 10.1007/s00348-014-1857-7.

[28] H. G. Maas, A. Gruen, and D. Papantoniou. "Particle tracking velocimetry in three-dimensional flows". In: *Experiments in Fluids* 15.2 (July 1, 1993), pp. 133–146. DOI: 10.1007/BF00190953.

[29] R. Meynart. "Instantaneous velocity field measurements in unsteady gas flow by speckle velocimetry". In: *Applied Optics* 22.4 (Feb. 15, 1983), p. 535. DOI: 10.1364/AO.22.000535.

[30] C. Mounaïm-Rousselle, L. Landry, F. Halter, and F. Foucher. "Experimental characteristics of turbulent premixed flame in a boosted Spark-Ignition engine". In: *Proceedings of the Combustion Institute* 34.2 (2013), pp. 2941–2949. DOI: https://doi.org/10.1016/j.proci.2012.09.008.

[31] F. T. M. Nieuwstadt, J. Westerweel, and B. J. Boersma. *Turbulence: Introduction to Theory and Applications of Turbulent Flows*. 1st ed. 2016. Cham: Springer International Publishing : Imprint: Springer, 2016. 1 p. DOI: 10.1007/978-3-319-31599-7.

[32] M. Novara, K. J. Batenburg, and F. Scarano. "Motion tracking-enhanced MART for tomographic PIV". In: *Measurement Science and Technology* 21.3 (Mar. 1, 2010), p. 035401. DOI: 10.1088/0957-0233/21/3/035401.

[33] J. R. Osborne, S. A. Ramji, C. D. Carter, S. Peltier, S. Hammack, T. Lee, and A. M. Steinberg. "Simultaneous 10 kHz TPIV, OH PLIF, and CH2O PLIF measurements of turbulent flame structure and dynamics". In: *Experiments in Fluids* 57.5 (Apr. 16, 2016), p. 65. DOI: 10.1007/s00348-016-2151-7.

[34] G. Pan and H. Meng. "Digital Holographic PIV for 3D Flow Measurement". In: *Fluids Engineering*. ASME 2002 International Mechanical Engineering Congress and Exposition. New Orleans, Louisiana, USA: ASMEDC, Jan. 1, 2002, pp. 43–49. DOI: 10.1115/IMECE2002-33173.

[35] N. Peters. *Turbulent Combustion*. 1st ed. Cambridge University Press, Aug. 15, 2000. DOI: 10.1017/CBO9780511612701.

[36] B. Peterson, E. Baum, B. Böhm, and A. Dreizler. “Early flame propagation in a spark-ignition engine measured with quasi 4D-diagnostics”. In: *Proceedings of the Combustion Institute* 35.3 (2015), pp. 3829–3837. DOI: 10.1016/j.proci.2014.05.131.

[37] B. Peterson, E. Baum, A. Dreizler, and B. Böhm. “An experimental study of the detailed flame transport in a SI engine using simultaneous dual-plane OH-LIF and stereoscopic PIV”. In: *Combustion and Flame* 202 (2019), pp. 16–32. DOI: https://doi.org/10.1016/j.combustflame.2018.12.024.

[38] L. Prandtl. *Entstehung von Wirbeln bei Wasserströmungen - 1. Entstehung von Wirbeln und künstliche Beeinflussung der Wirbelbildung*. 1936. DOI: 10.3203/IWF/C-1.

[39] M. Raffel, C. E. Willert, F. Scarano, C. J. Kähler, S. T. Wereley, and J. Kompenhans. *Particle Image Velocimetry: A Practical Guide*. Cham: Springer International Publishing, 2018. DOI: 10.1007/978-3-319-68852-7.

[40] B. E. Rice, J. A. McKenzie, S. J. Peltier, C. S. Combs, B. S. Thurow, C. J. Clifford, and K. Johnson. “Comparison of 4-camera Tomographic PIV and Single-camera Plenoptic PIV”. In: 2018 AIAA Aerospace Sciences Meeting. Kissimmee, Florida: American Institute of Aeronautics and Astronautics, Jan. 8, 2018. DOI: 10.2514/6.2018-2036.

[41] F. Scarano. “Tomographic PIV: principles and practice”. In: *Measurement Science and Technology* 24.1 (Oct. 2012), p. 012001. DOI: 10.1088/0957-0233/24/1/012001.

[42] D. Schanz, A. Schröder, S. Gesemann, D. Michaelis, and B. Wieneke. “‘Shake The Box’: A highly efficient and accurate Tomographic Particle Tracking Velocimetry (TOMO-PTV) method using prediction of particle positions”. In: *PIV13; 10th International Symposium on Particle Image Velocimetry*. Date: 01-03, July. Delft, The Netherlands, 2013, pp. 1–13.

[43] J. F. G. Schneiders and F. Scarano. “Dense velocity reconstruction from tomographic PTV with material derivatives”. In: *Experiments in Fluids* 57.9 (Sept. 2016), p. 139. DOI: 10.1007/s00348-016-2225-6.

[44] M. Stanislas, L. Perret, and J. Foucaut. “Vortical structures in the turbulent boundary layer: a possible route to a universal representation”. In: *Journal of Fluid Mechanics* 602 (May 10, 2008), pp. 327–382. DOI: 10.1017/S0022112008000803.

[45] UN The United Nations. *The Paris Agreement*. Paris: UNFCCC, Nov. 2015.

[46] M P. Tokarev, D K. Sharaborin, A S. Lobasov, L M. Chikishev, V M. Dulin, and D M. Markovich. “3D velocity measurements in a premixed flame by tomographic PIV”. In: *Measurement Science and Technology* 26.6 (June 1, 2015), p. 064001. DOI: 10.1088/0957-0233/26/6/064001.

[47] P. J. Trunk, I. Boxx, C. Heeger, W. Meier, B. Böhm, and A. Dreizler. “Premixed flame propagation in turbulent flow by means of stereoscopic PIV and dual-plane OH-PLIF at sustained kHz repetition rates”. In: *Proceedings of the Combustion Institute* 34.2 (2013), pp. 3565–3572. DOI: https://doi.org/10.1016/j.proci.2012.06.025.

[48] M. P. Wernet, A. Wróblewski, and R. J. Locke. *A Dual-Plane PIV Study of Turbulent Heat Transfer Flows*. Technical Report NASA/TM—2016-219074. Cleveland: Glenn Research Centre, 2016.

[49] J. Westerweel. *Digital particle image velocimetry: Theory and application*. Delft University Press, 1993. 236 pp.

[50] J. Westerweel and F. Scarano. “Universal outlier detection for PIV data”. In: *Experiments in Fluids* 39.6 (Dec. 1, 2005), pp. 1096–1100. DOI: 10.1007/s00348-005-0016-6.

[51] Frank M. White. *Fluid mechanics*. 7. ed. McGraw-Hill Series in Mechanical Engineering. New York: McGraw-Hill, 2011. 862 pp.

[52] B. Wieneke. “Volume self-calibration for 3D particle image velocimetry”. In: *Experiments in Fluids* 45.4 (Oct. 1, 2008), pp. 549–556. DOI: 10.1007/s00348-008-0521-5.

[53] N. A. Worth and T. B. Nickels. “Acceleration of Tomo-PIV by estimating the initial volume intensity distribution”. In: *Experiments in Fluids* 45.5 (Nov. 1, 2008), pp. 847–856. DOI: 10.1007/s00348-008-0504-6.

[54] Y. Zheng, L. Weller, and S. Hochgreb. “Instantaneous flame front identification by Mie scattering vs. OH PLIF in low turbulence Bunsen flame”. In: *Experiments in Fluids* 63.5 (May 5, 2022), p. 79. DOI: 10.1007/s00348-022-03423-8.

A

Data Tables

A.1. Seeding Densities

The calculation of the seeding density as explained in section 4.2.3, applied to the most successful experimental runs. There is a good spread of seeding across the experiments.

Case & Run Number	Seedling level	Particles per Pixel (ppp)
Case 3 & Run 2	Medium	0.027
Case 3 & Run 6	Low	0.014
Case 3 & Run 7	High	0.056
Case 4 & Run 1	Low	0.012
Case 4 & Run 2	Low	0.013
Case 4 & Run 3	Medium	0.028
Case 4 & Run 5	Medium	0.026
Case 4 & Run 6	Medium	0.028
Case 4 & Run 7	Medium	0.038
Case 4 & Run 8	High	0.059
Case 4 & Run 9	High	0.078
Case 4 & Run 10	High	0.072

Table A.1: Seeding level (Low-High) defined visually and Seeding density (0.01-0.08ppp) defined by particle counting in set windows. Both levels given for every run of significance in the 3mm light sheet experiments.

A.2. Experiment Means and Standard Deviations

The dimensionless standard deviations of each divergence plot as referenced in section 4.2 are displayed in the table below for each filter radius length that was tested. The mean of each run was also calculated.

Case & Run Number	Filter	Mean	Standard Deviation
Case 3 & Run 2	2	-0.0844	1.6256
	3	-0.0576	1.0633
	4	-0.0490	0.7046
	5	-0.0546	0.4985
	6	-0.0619	0.3889
Case 3 & Run 6	2	-0.0215	1.5033
	3	-0.0059	0.9710
	4	0.0003	0.6304
	5	-0.0008	0.4370
	6	-0.0041	.0.3374
Case 3 & Run 7	2	-0.1402	1.7672
	3	-0.1178	1.1398
	4	-0.1047	0.7494
	5	-0.1067	0.5376
	6	-0.1107	0.4346
Case 3 & Run 8	2	-0.1862	1.8978
	3	-0.1614	1.2386
	4	-0.1501	0.8254
	5	-0.1504	0.5956
	6	-0.1540	0.4781
Case 4 & Run 1	2	-0.0978	1.1343
	3	-0.0717	0.7320
	4	-0.0587	0.4824
	5	-0.0567	0.3377
	6	-0.0610	0.2548
Case 4 & Run 2	2	-0.1441	1.2621
	3	-0.1105	0.8158
	4	-0.0934	0.5385
	5	-0.0912	0.3810
	6	-0.0987	0.2964

Table A.2: Table of non-dimensionalised standard deviations and means of divergence fields included in the 3mm light sheet experiments. (Part 1)

Case & Run Number	Filter	Mean	Standard Deviation
Case 4 & Run 3	2	-0.1187	1.3970
	3	-0.0969	0.9094
	4	-0.0841	0.6118
	5	-0.0834	0.4457
	6	-0.0891	0.3574
Case 4 & Run 5	2	-0.1261	1.2022
	3	-0.1113	0.7878
	4	-0.1036	0.5317
	5	-0.1044	0.3866
	6	-0.1111	0.3101
Case 4 & Run 6	2	-0.1118	1.1193
	3	-0.0969	0.7332
	4	-0.0815	0.4939
	5	-0.0806	0.3568
	6	-0.0873	0.2801
Case 4 & Run 8	2	-0.0938	1.4042
	3	-0.0807	0.9112
	4	-0.0738	0.6072
	5	-0.0748	0.4387
	6	-0.0764	0.3485
Case 4 & Run 9	2	-0.1359	1.1306
	3	-0.1177	0.7455
	4	-0.1104	0.5024
	5	-0.1133	0.3634
	6	-0.1174	0.2843
Case 4 & Run 10	2	-0.0790	1.0484
	3	-0.0577	0.6933
	4	-0.0498	0.4739
	5	-0.0516	0.3507
	6	-0.0563	0.2849

Table A.3: Table of non-dimensionalised standard deviations and means of divergence fields included in the 3mm light sheet experiments. (Part 2)

B

Hydrogen Experiment Results

A sample divergence plot for a predominately hydrogen fuelled run. The data shows very similar to results as to the ones seen in section 4.2, although due to time constraints there is less data populated in this figure. Interesting runs with lower seeding levels appear to be much more accurate than with higher seeding, typical for tomographic PIV but not what was seen in the natural gas fuelled runs.

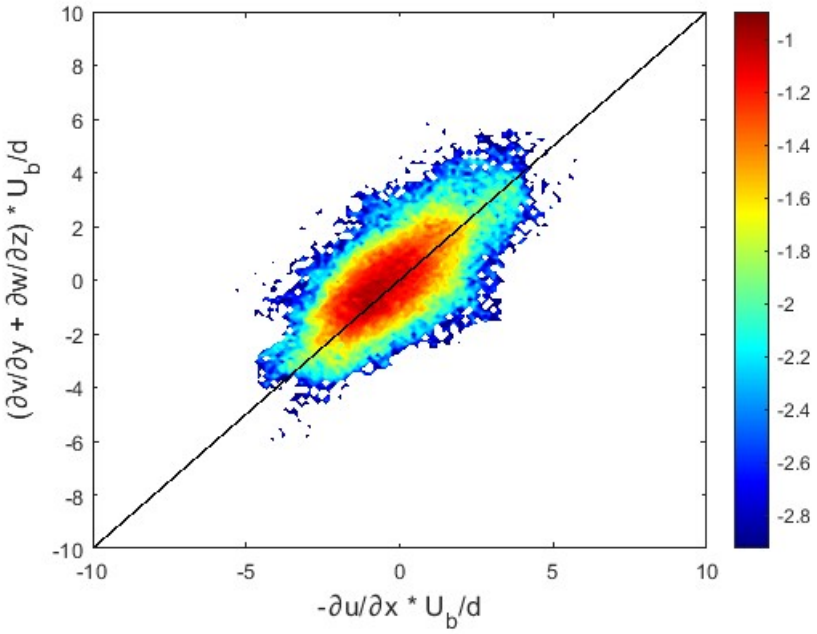

Figure B.1: Joint pdf of divergence components ($-du/dx$) and ($dv/dy + dw/dz$). The contours are in log scale. The black line indicates zero divergence, any deviation from the diagonal indicates measurement error. The further from the centre line the more error present. Experimental Conditions: Low seeding ($\sim 0.02ppp$), Time Separation (Δt = 45μs) and a linear filter radius length of 5.